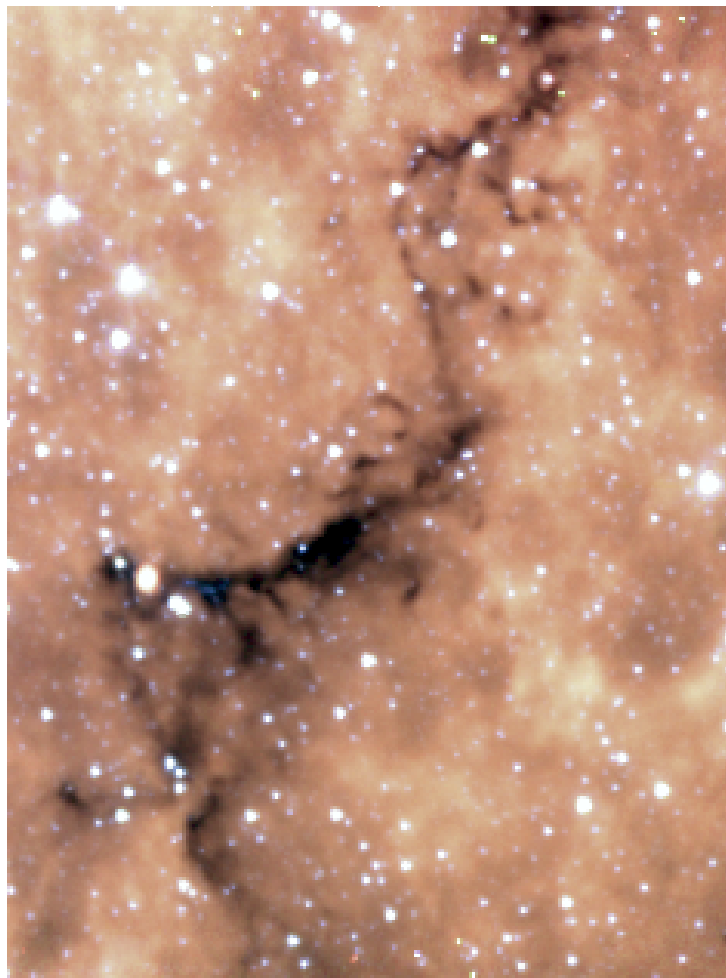


The Evolutionary State of Young Stellar Objects in IRDC G48

Matthijs H.D. van der Wiel

Groot Onderzoek (master thesis) at the Kapteyn Astronomical Institute, University of Groningen
Supervisor: Russell F. Shipman

April 10, 2007



Abstract

Spitzer Space Telescope mid-infrared (3–24 μm) photometry is processed and analyzed in order to assess the young stellar content of Infrared Dark Cloud G48. It is established from color-color diagram analysis that ~ 40 objects are YSO (Young Stellar Object) candidates, spread out over all phases of YSO evolution. One third of these sources are classified in the early envelope accretion phase. SED (Spectral Energy Distribution) model fitting identifies seven of the twenty 24 μm cores as YSOs, again in varying stages of evolution. SED model fitting places the masses of the central stellar objects of the cores in the range 2.5–14 M_{\odot} . The sub-millimeter core ‘P1’ (Ormel et al. 2005) is broken up into two cores by Spitzer observations; SED model fitting to these two cores is consistent with the total central luminosity of 10^2 – $10^3 L_{\odot}$ found by previous modeling.

Contents

1	Introduction	3
1.1	Physics of star formation	3
1.2	Classification of protostars	3
1.2.1	SED slope	3
1.2.2	Color indices	4
1.2.3	Full spectral energy distributions	4
1.3	Infrared dark clouds	4
1.4	IRDC G48	5
1.5	Goal	5
2	Data reduction	6
2.1	Observations	6
2.2	Image processing	6
2.2.1	Constructing mosaics with MOPEX	6
2.2.2	IRAC point source extraction	6
2.2.3	MIPS point source extraction	8
2.2.4	Aperture photometry	8
2.3	Flux and magnitude calibration	8
2.4	Flux and magnitude uncertainty	8
2.5	Band merging	9
2.5.1	Matching bands by position	9
2.5.2	Filtering the list	9
2.5.3	Merged list	10
2.6	Final source list	10
3	Comparison to IRAC sources from GLIMPSE	11
3.1	Properties of GLIMPSE	11
3.2	Comparison to our data	11
3.3	Fixing the discrepancy	12
4	YSO models	13
4.1	The YSO model grid	13
4.1.1	Advantages	13
4.1.2	Caveats	13
4.2	Stage classification	14
5	Analysis and results	15
5.1	Color-color diagrams	15
5.1.1	Stage I objects	15
5.1.2	Disk objects	15
5.1.3	Possible photospheres	15
5.1.4	Blue objects in [3.6] – [4.5]	17
5.1.5	IRAC+MIPS colors	17
5.2	SED fitting	18
5.2.1	SED fitting tool	18
5.2.2	Brightest cores	19
5.2.3	Fitting other cores	21
5.2.4	Lack of datapoints for nine MIPS cores	24
5.2.5	Summary of SED fitting results	24
6	Discussion	25
6.1	Contamination of YSO sample	25
6.1.1	AGB stars	25
6.1.2	Extincted photospheres	25
6.1.3	Background galaxies	25
6.2	Mid-IR counterparts of P2 and EP	26
6.3	Future work	26
7	Conclusions	26
A	List of acronyms	27

1. Introduction

1.1. Physics of star formation

The formation of stars is generally accepted to start from the fragmentation of molecular clouds (Shu et al. 1987). As a cloud becomes gravitationally unstable and is able to cool (through molecular lines), it collapses and fragments further. This fragmentation is observed to occur down to all size scales, giving rise to the broad variety in emergent stellar masses. Once the cloud condenses into cold ‘cores’ of dense molecular gas and dust, the gravitational collapse process sets in towards the formation of a protostar (Rathborne et al. 2006). The overall mass accretion rate is highest in the first phase of star formation (which generally lasts $\sim 10^4$ yr) and is assumed to decrease with time (Klessen 2001).

The subsequent phases of star formation are generally believed to occur through more accretion from the circumstellar envelope onto a rotating circumstellar disk. In the meantime, the central protostar heats up and starts emitting copious amounts of energy, which leads to bipolar outflow jets and cavities in the envelope. As time progresses, the mass of the disk grows through accretion from the envelope (which becomes thinner in the process) and the mass of the central star grows through disk accretion. The point at which the disk becomes the dominant dynamical component is a few $\times 10^5$ yr after the central star has turned on (Klessen 2001). The disk is heated and partly evaporated by the central star, imposing a flared disk geometry. Finally, the disk is partly accreted onto the central star and partly evaporated and the photosphere of the star becomes visible from all viewing angles (White et al. 2007). The entire process from protostellar contraction to the ‘naked’ photosphere on the main sequence is estimated to last in the order of 10^6 yr.

The general effect of circumstellar material around a young star on the spectral energy distribution (SED¹) is that the near-IR and optical photons from the photosphere are absorbed by the disk and envelope and are subsequently re-radiated by the hot dust at longer wavelengths. The exact regime in which photons are re-radiated depends on the acquired temperature of the dust. Moreover, part of the emission of a young stellar object (YSO) is due to accretion luminosity, arising from dust and gas from the circumstellar components impacting on the star.

For low-mass stars ($\lesssim 5 M_{\odot}$), observations have confirmed the evolutionary phases of accretion of material from the environment, subsequent disk formation and bipolar outflows and jets. The earliest phases of this mode of star formation are identified as Bok globules (Bok & Reilly 1947). These generally isolated spots stand out in optical extinction. They are found to have masses ranging from 1–100 M_{\odot} , sizes of less than 2 parsec and pre-protostellar cores (~ 0.05 parsec) with low temperatures (~ 10 K), high densities (10^5 – 10^6 cm^{-3}) and core masses in the range 0.5–5 M_{\odot} .

Where low-mass star formation occurs in isolated regions, high-mass star formation on the other hand, occurs in much more clustered environments (e.g. Rathborne et al. (2006); Lada & Lada (2003)). High-density cores (10^5 – 10^8 cm^{-3}) heavily obscure the early phase of high-mass star formation, particularly at optical and near-IR wavelengths. In addition, high-mass stars are rare, so it is statistically more difficult to observe them. Therefore, direct observations of high-mass protostars are limited and the understanding of high-mass star formation lags behind on the low-mass equivalent (Evans 1999). The general pic-

ture sketched above is taken to be true for all modes (low-mass to high-mass) of star formation.

1.2. Classification of protostars

In order to make an observational distinction between the various phases of star formation, observable parameters must be connected to the physical state of an object. A variety of methods exists to come to an observational classification of YSOs.

1.2.1. SED slope

The very first phase of star formation is often referred to as ‘Class 0’, where the SED resembles a 30 K graybody at sub-mm wavelengths, showing little or no excess emission at near- and mid-IR wavelengths. Traditionally, the subsequent phases of YSOs are classified using the slope of the SED between roughly $2 \mu\text{m}$ and $25 \mu\text{m}$, usually defined as:

$$\alpha = \frac{d \log_{10} \lambda F_{\lambda}}{d \log_{10} \lambda} \quad (1)$$

Evolution of a protostar is taken to have a monotonic effect on this SED slope, α , (White et al. 2007; Adams et al. 1987). A ‘Class I’ source ($\alpha > 0$) is generally accepted to be a source which is embedded in an accreting envelope. In the next phase, ‘Class II’, where $-2 < \alpha < 0$, a source would be considered a disk source. This phase of a protostar is also commonly designated as the T Tauri phase (White et al. 2007). Finally, around a ‘Class III’ source, with $\alpha < -2$, only a very optically thin debris disk would remain. As a protostar evolves, the circumstellar material is dispersed and evaporated, and more and more of the photosphere of the star becomes directly visible. The general trend is that the younger the object, the higher α in the 2–25 μm range.

However, the effect on α of the evolution of a protostar through time is not as simple as sketched above. The shape of the SED depends on a combination of parameters that describe the protostar and its surrounding disk, envelope and ambient environment. In addition, the viewing angle at which a YSO is observed is an important parameter: parts of the circumstellar material may be obscuring the central source and therefore affect the shape of the SED. For example: observing an object at an edge-on inclination, through the plane of the disk, obscures the central source and results in much indirect radiation from the heated dust. Looking at the same source face-on, when a significant part of the total SED is determined by direct radiation from the protostar, would result in a very different SED. This is readily shown by the models of Whitney et al. (2003) in Fig. 2, where the theoretical equivalents of the observationally defined ‘Classes’ are translated into SEDs. First of all, it is evident that the slope of the SED in the 2–25 μm regime cannot be described by one parameter, since the slope changes with wavelength even within this regime. Second, even if this slope is somehow determined, it is evidently not uniform within a Class. Fig. 2 shows that the SED shape depends greatly on viewing angle, and this is only one of many parameters that may vary within a class of objects.

The conclusion is that the evolutionary phase of the YSO (time) as the only factor that determines its SED shape is a gross oversimplification (see e.g. Whitney et al. (2003), White et al. (2007)). There is a wide range of parameters responsible for the physical processes in and around the protostar (the central source, disk and envelope parameters) and those that deter-

¹ A list of acronyms can be found in Appendix A on page 27.

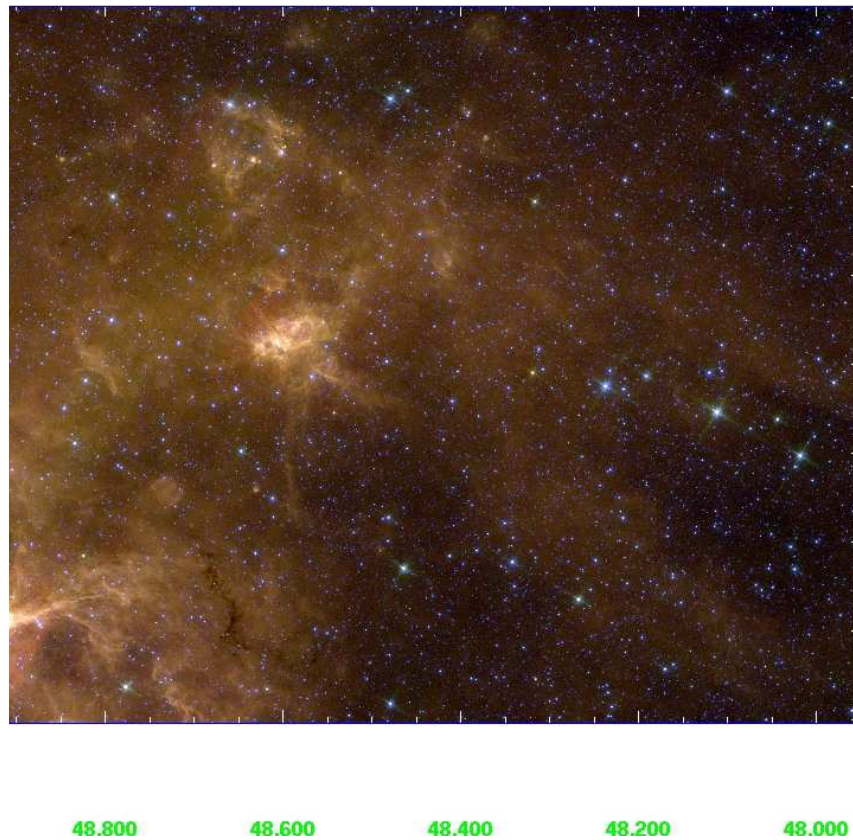


Fig. 1. Three-color composite image (IRAC 3.6 μm , 5.8 μm and 8.0 μm) from GLIMPSE (Benjamin et al. 2003). The coordinates are galactic latitude (b) along the vertical axis and galactic longitude (l) along the horizontal axis. Infrared dark cloud G48 is visible as a dark filamentary patch at $(l, b) = (48^\circ.65, -0^\circ.3)$.

mine how energy is transported to the observer (e.g. the viewing angle). A new classification scheme is therefore proposed by Robitaille et al. (2006), which is described in Sec. 4.2.

1.2.2. Color indices

An improvement on the ‘Class’ scheme described above is to consider multiple color indices. Once fluxes of an object are measured in various bands at different wavelengths, relative fluxes can be examined in a *range* of wavelengths, instead of the intercomparison of only 2 and 25 μm . Relative fluxes are generally expressed in terms of the difference between two magnitudes: a *color index*. If one is now able to define two different color indices (from fluxes in at least three different bands), the locus of the object in a color-color diagram can be derived. Examples of color-color diagrams are extensively discussed in Sec. 5.1.

1.2.3. Full spectral energy distributions

Classifying an object by examining its complete SED is the most detailed assessment one could make. The advantage of considering the complete SED is that the analysis of the object is not constrained to properties in very specific wavelength regions. For example, color-color diagrams are usually constructed from color indices closely spaced in wavelength space, e.g. U–B

vs. B–V or J–H vs. H–K. In a full SED examination, the properties of a source at all wavelengths can ideally be studied at once. However, this is not always possible in practice due to lack of datapoints at specific wavelengths, resulting in degenerate results in terms of possible SED shapes. Examples of SED studies of individual objects are shown in Sec. 5.2.

1.3. Infrared dark clouds

It has been suggested that regions of massive star formation, the high-mass counterparts of Bok globules, are the so-called Infrared dark clouds (IRDCs). IRDCs were discovered independently by Perault et al. (1996) and Egan et al. (1998) as dark patches against the Galactic mid-IR background. High column densities (10^{23} – 10^{25} cm^{-2}) of dust absorb the mid-IR radiation. The molecular temperatures in IRDCs are < 25 K and volume densities are $> 10^5$ cm^{-3} (Egan et al. 1998; Carey et al. 2000). IRDCs are generally not quiescent, they harbor compact cores of sub-millimeter emission, as shown by e.g. Ormel et al. (2005); Carey et al. (2000); Rathborne et al. (2005).

IRDCs are found primarily in the inner Galaxy and close to the Galactic plane (Carey et al. 2000). There are already thousands of known IRDCs (Simon et al. 2006a) in the first and fourth quadrants of the Galactic plane, i.e. the inner Galaxy. Efforts are being made to find IRDC counterparts in the outer

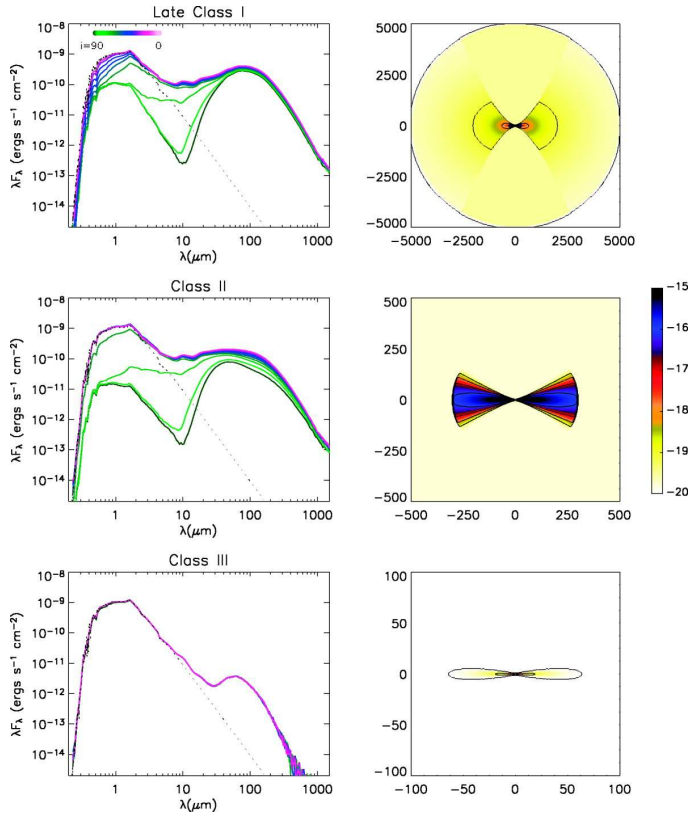


Fig. 2. The SEDs (left) and density structures (right) of Class I, II and III (from top to bottom) young stellar objects as modeled by Whitney et al. (2003). The colored SEDs indicate different inclination angles with respect to the line of sight, ranging from dark green for 90° (edge-on) to pink for 0° (pole-on). The density scale for the density structures is logarithmic. The size range is indicated along the axes in AU.

galaxy (Frieswijk et al. 2005), requiring a completely different detection technique in the absence of bright mid-IR background.

1.4. IRDC G48

The IRDC under investigation in this thesis is the cloud at galactic coordinates $(\ell, b) = (48^\circ.65, -0^\circ.3)$. In the dark cloud catalog of Simon et al. (2006a), this cloud has the designation ‘MSXDC G048.65–00.29’; it will be called ‘G48’ throughout this thesis. Its distance is determined kinematically from molecular line data and an assumed Galactic rotation curve. G48 is found to be at a distance of ~ 2.5 kpc (Ormel et al. 2005; Simon et al. 2006b). Its distance to the Galactic Center is ~ 7 kpc and it is less than 20 pc away from the mid-plane of the Galaxy. Its total mass is estimated at almost $600 M_\odot$ within a 2 pc area and the molecular (H_2) density is $\sim 10^3 \text{ cm}^{-3}$ (Simon et al. 2006b). Precisely these high molecular densities and total masses typical for IRDCs make them candidates for high-mass star formation regions. Ormel et al. (2005) identified three distinct emission cores at 450 and 850 μm and determined central luminosity sources in two of these cores in the order of 10^2 – $10^3 L_\odot$.

This IRDC has been previously observed by the Mid-course Space Experiment (MSX), the SCUBA instrument on the JCMT (Ormel et al. 2005), the Infrared Astronomical Satellite (IRAS) and by the JCMT spectrograph (Shipman et al. 2003). In addition, it is covered by GLIMPSE (the Galactic Legacy Infrared Mid-Plane Survey Extraordinaire, see Benjamin et al. (2003)); a

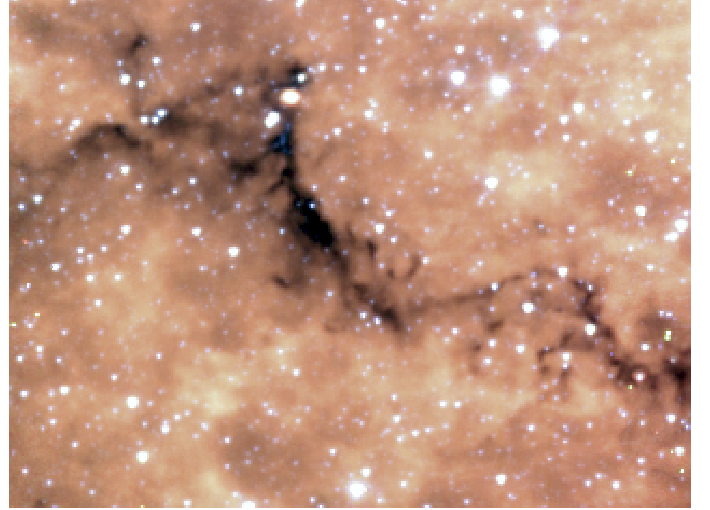


Fig. 3. Three-color composite image of IRDC G48, composed of data of three of the Spitzer passbands discussed in this thesis: 3.6 μm (blue), 4.5 μm (green) and 8.0 μm (red).

large mosaic image from the archive, showing the surroundings of G48, is given in Fig. 1.

1.5. Goal

The work in this thesis focuses on newly obtained deeper mid-IR images of G48, using two instruments on board the *Spitzer Space Telescope*: all four bands of the InfraRed Array Camera (IRAC), covering the range 3–10 μm , and one band of the Multiband Imaging Photometer for Spitzer (MIPS), centered around 24 μm .

The goal of this project is to determine the evolutionary phases of the young stellar objects associated to the IRDC and to assess the state of star formation in the cloud as a whole. The *Spitzer Space Telescope* photometry of the cloud was obtained in order to study the sources near and in the IRDC at mid-IR wavelengths. These observations are processed and interpreted here.

2. Data reduction

2.1. Observations

The images of Infrared Dark Cloud (IRDC) G48 were recorded in October 2004 by the Infrared Array Camera (IRAC) and Multiband Imaging Photometer (MIPS) on board the *Spitzer Space Telescope*.

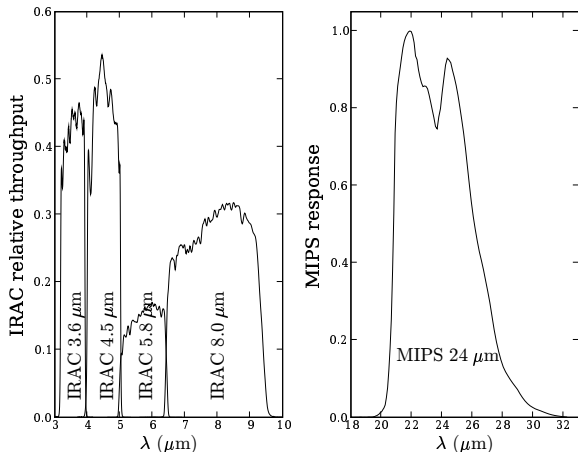


Fig. 4. Transmission curves for the four IRAC wavebands (left) and for the MIPS 24 μm band (right).

Photometric images were obtained in five bands: all four bands of IRAC (centered around 3.6, 4.5, 5.8 and 8.0 μm) and the first band of MIPS (24 μm). The bandwidths of the IRAC bands are approximately $\frac{1}{4}$ of the central wavelength (0.75 μm for IRAC 3.6 and almost 3 μm for IRAC 8.0), see Fig. 4.

For the IRAC bands, the 12 second High Dynamic Range mode is used: ten dithered images of 10.4 s and ten of 0.4 s, adding up to a total integration time of 104 seconds per IRAC band. IRAC observes two adjacent $5' \times 5'$ fields simultaneously, MIPS observes only one at a time. MIPS images are also dithered, a total of 44 images spread over the two fields add up to an integration time of 55 s per field. The resolution in band 1 of IRAC is limited by the pixel size of the CCD ($\sim 1''.2$); it is diffraction limited for the higher wavelengths, with the resolution element ranging from $1''.3$ for IRAC 4.5 μm to $6''$ for the 24 μm MIPS band (Rieke et al. 2004; Fazio et al. 2004).

At a galactic longitude of $48^\circ.6$, IRDC G48 lies close to the line of sight towards the giant molecular cloud W51 and is located at a galactic latitude of only $-0^\circ.3$. At a position like this — in the galactic plane — there is significant background radiation.

The Spitzer Science Center (SSC) provided ‘basic calibrated data’ in units of physical flux per unit solid angle. The basic calibrated data, originating from pipeline version S11.4.0 in case of IRAC and version S10.5.0 for the MIPS band, include uncertainty images and bad pixel maps. The processing of these images is described in Section 2.2, the calibration is described in Section 2.3.

2.2. Image processing

2.2.1. Constructing mosaics with MOPEX

The software package MOPEX (MOsaicing and Point source EXtraction, version 030106, see Makovoz & Marleau (2005)) is

chosen as the primary tool for the data analysis. The package is being developed² by the Spitzer Science Center (SSC) with the aim of exploiting and incorporating the specific nature of *Spitzer* data. The properties of the images vary in a number of parameters: from undersampled 3.6 μm images to highly oversampled 24 μm images; from very low background and large probability of source confusion at the shortest wavelengths to highly variable and dominant background structure at the longest wavelengths. These issues are all the more important considering the line of sight in the Galactic plane towards the inner Galaxy.

Before performing the point source extraction, the IRAC images are processed by other MOPEX scripts: to remove mux bleed and column pulldown artefacts; to replace the saturated parts of the long exposures (10.4 s) by their counterparts from the short (0.4 s) exposures; to perform pointing refinement³ and finally to combine individual frames into one mosaic per band (Makovoz & Khan 2005). The bad pixel maps are used as additional input for the mosaic script, in order to ensure that the result is not influenced by these detector artefacts. Every mosaic is accompanied by an uncertainty mosaic, constructed from the individual uncertainty images provided by the SSC.

The MIPS images are combined into a mosaic by the same script that was used for the IRAC images. The result is shown in the last panel of Fig. 5.

The field of view for Spitzer imaging is $5' \times 5'$ for every individual frame. Due to the offset in the fields of view for IRAC bands 1 and 3 relative to bands 2 and 4, Spitzer’s capability of simultaneously observing in two bands and dithering of the observations, the combined mosaic images have fields of view slightly larger than two adjacent $5' \times 5'$ squares.

Of each mosaic, only the region that overlaps with the other wavelength bands (approximately $5' \times 5'$, about half of the total mosaic) is shown in Fig. 5.

2.2.2. IRAC point source extraction

Once the mosaic images have been constructed, these can be used as input to the MOPEX single frame point source extraction algorithm (Makovoz & Marleau 2005), in combination with an uncertainty mosaic image and a coverage map. It consists of two main processes: point source detection and subsequent profile fitting. The first step produces a list of candidate point sources. Background subtracted and noise images are created to use for the point source fitting and for computing S/N ratios for the point sources, respectively. The second step fits a specified profile (in this case the PRF provided by the SSC) to all candidate sources from the first step, further improving the accuracy of the positions of the sources and estimates of their fluxes. The result is a table of sources listing positions with uncertainties, fluxes with uncertainties (see Section 2.3 for a discussion of the flux calibration) and S/N ratio, among other things.

The above routine is performed twice for every band. The first run through the point source extraction routine is done primarily to find a number of clean (reduced $\chi^2 < 50$), well-detected ($S/N > 50$) sources. A further selection of isolated sources is made by hand, to be used in the construction of an empirical PRF. This new PRF is used to run the mosaic image

² The first version of the package was released in September 2005, the next version in March 2006 (the version used in this project) and a graphical user interface has just been released in early 2007.

³ This is done in order to increase the accuracy of the pointing in one image frame relative to another, with the goal of producing more accurate mosaics when individual frames are combined.

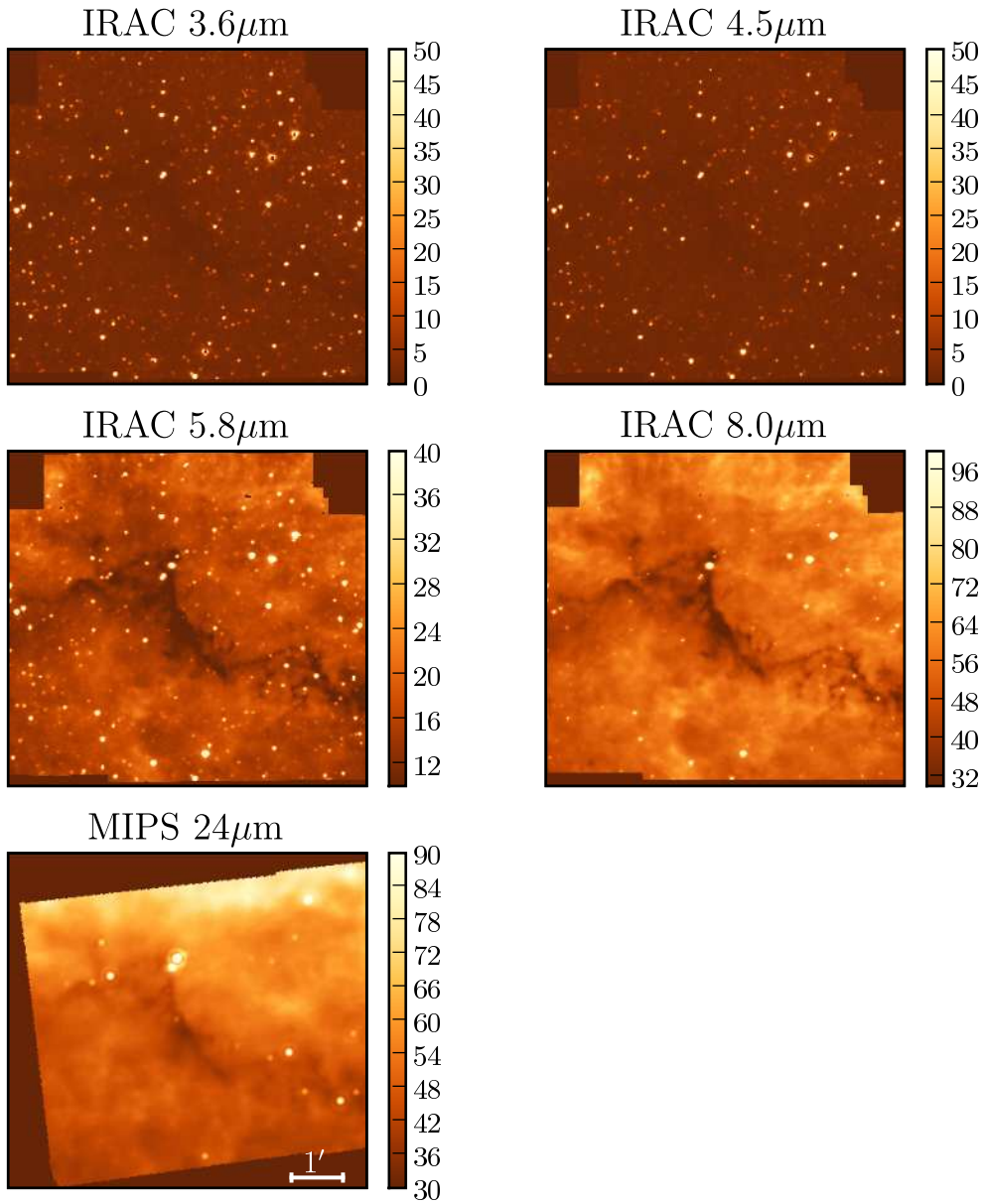


Fig. 5. The mosaics for the four IRAC bands and the MIPS $24\ \mu\text{m}$ band, obtained by the method described in Sec. 2.2.1. The scale is the same in all five images. The scale bar in the MIPS image indicates one arcminute, which corresponds to ~ 0.7 parsec at the distance of 2.5 kpc. The brightness scales vary from one band to the other and are in units of MJy/sr. Of every mosaic, only the region where overlapping data is available in all five bands is shown; this is approximately half of the total mosaic.

through the source extractor a second time. The successfully fitted sources from this last run are put in four tables, one for every band. Applying a signal-to-noise limit of 5, a total of 1622, 1113, 464 and 203 point sources are extracted in IRAC 3.6, IRAC 4.5, IRAC 5.8 and IRAC 8.0, respectively.

Before settling on the final method (the seventh different run of the software) and the above mentioned tables, the extracted point sources from every run are checked against corresponding sources from the GLIMPSE survey (see Chapter 3). Parameters

in the extraction routines are progressively better understood and adapted in order to improve the result.

The extraction described above is done on the complete mosaics of $\sim 5' \times 10'$. However, due to shifts in the fields of view from one band to the other, the area for which there is information in all bands is $\sim 5' \times 5'$ (see also Section 2.5). The total numbers of point sources listed above are roughly cut in half when only the overlapping area is taken into account.

2.2.3. MIPS point source extraction

The starting point for point source extraction in the MIPS 24 μm band differs from IRAC in two respects. First of all, there are fewer sources in the MIPS image, which reduces the odds of finding blended sources. Secondly, due to galactic emission around 24 μm (e.g. by PAH molecules) the background is even more variable than in the IRAC bands, providing for more difficulties in the automated fitting and extraction of point sources.

Constructing a new PRF from the input mosaic does not improve the source extraction in the MIPS band, so in this case the MOPEX extraction (see Section 2.2.2 for a description of the MOPEX point source extractor) uses only the PRF provided in the calibration directory of basic calibrated data. Selecting the successfully fitted sources results in a list of fourteen MIPS sources, three of which fall outside the area that overlaps with all IRAC observations. Like for IRAC, the table includes positions with uncertainties, fluxes with uncertainties (see Section 2.3 for a discussion of the flux calibration) and S/N ratio. The signal-to-noise criterion is the same as for the IRAC bands: $S/N > 3$. This is somewhat arbitrary, since all fourteen resulting sources have S/N of at least 20. The determination of positions and fluxes of ten additional MIPS sources is described in Section 2.2.4.

2.2.4. Aperture photometry

An overlay of the coordinates of sources extracted by MOPEX in MIPS 24 μm and IRAC 8.0 μm (see Sections 2.2.2 and 2.2.3) on top of the corresponding images shows that about a dozen obvious sources are missing from each list. They have not been picked up by the PRF fitting routine, possibly due to a combination of low flux of these sources and the particularly variable background in which they reside.

Almost no confusion of sources occurs at these wavelengths, which makes it possible to perform aperture photometry. Twelve previously unextracted sources in IRAC 8.0 and ten in MIPS are selected by eye. A separate script, independent of MOPEX, is developed to perform the aperture photometry. The positions of the selected sources are fed to this script.

Although it is not possible to fit a PRF to these sources, the position of every source can be determined to a sub-pixel precision by fitting a radial profile with standard functions in IRAF. This puts most position uncertainties at $\sim 0.7''$ in both bands. The position of only three very faint sources is more difficult to determine, raising their position uncertainty to values up to $1.8''$.

Most of the aperture photometry detections have a background value that is relatively well determined by the median of a surrounding annulus. Therefore, the fairly modest relative flux uncertainty (σ_F/F) of 10% is adopted. In a handful of cases where the annulus median does not produce a sound background value, the background needs to be set by hand. For these sources, the uncertainty in the flux is accepted to be larger: 50%. The calibration for the flux values is discussed in Section 2.3.

For the aperture photometry, only the sections of the images where information is available in all five bands are considered. Twelve sources are added to the IRAC 8.0 list, previously containing about one hundred sources. In MIPS, nine sources are extracted by aperture photometry, bringing the MIPS list to a total of 20 sources.

2.3. Flux and magnitude calibration

MOPEX fits a profile to a possible source detection (see also Section 2.2.2) by comparing all pixel values in the relevant part

Table 1. Zero magnitude fluxes for all IRAC bands and MIPS 24 μm .

band b	$F_{\text{zero}}^{[b]}$ (Jy)
IRAC 3.6 μm	280.9 \pm 4.1
IRAC 4.5 μm	179.7 \pm 2.6
IRAC 5.8 μm	115.0 \pm 1.7
IRAC 8.0 μm	64.13 \pm 0.94
MIPS 24 μm	7.14 \pm 0.0815

Table 2. Faintest and brightest sources detected by MOPEX.

band	faintest source		brightest source	
	flux (mJy)	mag	flux (mJy)	mag
IRAC 3.6 μm	0.072	16.5	142.8	8.2
IRAC 4.5 μm	0.12	15.4	162.2	7.6
IRAC 5.8 μm	1.3	12.4	189.9	7.0
IRAC 8.0 μm	3.5	10.7	141.2	6.6
MIPS 24 μm	8.2	7.3	121.8	4.4

of the input image to a PRF with two free parameters, the center and the peak value, and minimizing χ^2 (Makovoz & Marleau 2005). Key values from the FITS header related to the base unit and coordinate transformation⁴ are used to convert the integrated surface brightness (in units of MJy/sr) to a physical flux for a point source in μJy .

The flux calibration for the sources extracted by aperture photometry (see Section 2.2.4) is scaled such that the fluxes of a range of MOPEX extracted sources agree with the aperture photometry fluxes of the same sources. The sources only extracted by aperture photometry use the same scaling factor.

Magnitudes in the *Spitzer* bands are generally referred to as the central wavelength in micrometers, enclosed in square brackets: e.g. [3.6] denotes the magnitude in the IRAC 3.6 μm band. The fluxes $F^{[b]}$ (in mJy) in band b are converted to magnitudes by

$$[b] = -2.5 \log_{10} \left(\frac{F^{[b]}}{F_{\text{zero}}^{[b]}} \right), \quad (2)$$

where the magnitude $[b]$ is [3.6], [4.5], [5.8], [8.0] or [24] and $F_{\text{zero}}^{[b]}$ is the zero magnitude flux in band b in the same unit as $F^{[b]}$. Values and uncertainties for the zero magnitude fluxes are listed in Table 1. The zero magnitude flux for MIPS is retrieved from the SSC website⁵; those for IRAC are defined in Reach et al. (2005). The magnitude definition for IRAC and MIPS is an extension of the Vega-based magnitude system commonly used in the optical regime, where magnitude zeropoints are defined such that Vega (an A0-star) has magnitude 0 in all bands.

The faintest and brightest sources extracted by MOPEX in every band are listed in table 2. The faintest sources give an indication of the detection limits.

2.4. Flux and magnitude uncertainty

The uncertainty in the fluxes is determined from the MOPEX output, taking into account the PRF fitting uncertainty σ_{PRFfit} (generally of the order of percents of the total estimated flux) as well as the uncertainty due to general background noise, σ_{bg} . The latter is taken to be simply the noise factor from the S/N ratio. To get σ_{bg} , the estimated flux F of a source is divided by

⁴ Specifically the values connected to the keywords BITPIX, NAXIS, NAXIS1, NAXIS2, CRVAL1, CRVAL2, CRPIX1, CRPIX2, CTYPER1, CTYPER2, CDELT1, CDELT2, CROTA2 and BUNIT

⁵ <http://ssc.spitzer.caltech.edu/mips/calib/>

its S/N ratio, both of which are listed in the output table of the MOPEX point source extractor:

$$\sigma_{\text{bg}} = \frac{F}{S/N}. \quad (3)$$

The total uncertainty in a flux value is set to the quadratic sum of the two contributions:

$$\sigma_F = \sqrt{\sigma_{\text{PRFfit}}^2 + \sigma_{\text{bg}}^2}. \quad (4)$$

The contribution of σ_{bg} is most significant in the higher wavelength bands, where the background level is highly variable, which leads to a high noise level. At 3.6 and 4.5 μm , σ_{PRFfit} is by far the dominant term.

For the IRAC 8.0 μm and MIPS sources that are extracted by aperture photometry, values for σ_F are adopted at once, without taking into account two separate contributions. In the majority of the aperture photometry cases, σ_F is set to 10% of the flux F , and to 50% in some cases where the background level is not well-constrained (see Sec. 2.2.4). In fact, in discerning cases where 50% is used instead of 10%, separate contributions to the total flux uncertainty are implicitly incorporated.

The uncertainties in the fluxes, $\sigma_{F^{[b]}}$, and in the zero magnitude fluxes, $\sigma_{F_{\text{zero}}^{[b]}}$, are propagated to the magnitude uncertainties $\sigma_{[b]}$ through

$$\sigma_{[b]} = \frac{2.5}{\ln 10} \sqrt{\left(\frac{\sigma_{F^{[b]}}}{F^{[b]}}\right)^2 + \left(\frac{\sigma_{F_{\text{zero}}^{[b]}}}{F_{\text{zero}}^{[b]}}\right)^2}. \quad (5)$$

The second term in this equation – the relative uncertainty in the zero magnitude flux – is approximately 0.015 for all five bands. The first term – the relative uncertainty in the flux – is generally larger than the second term, especially in IRAC 5.8 μm , 8.0 μm and MIPS. These two contributions together constitute the magnitude uncertainty in Eq. 5.

The resulting magnitude uncertainties are of the order of 0.03, 0.04, 0.11 and 0.14 (median values) for the four IRAC bands in order of increasing wavelength. The complete distribution of magnitude uncertainties in every band is shown in Fig. 6. Of the IRAC 3.6 μm and IRAC 4.5 μm sources respectively, only 1% and 5% have magnitude uncertainties larger than 0.1. Of the IRAC 5.8 μm and IRAC 8.0 μm sources respectively, 3% and 5% have magnitude uncertainties larger than 0.22. The higher median and threshold magnitude uncertainties in the 8.0 μm band are partly due to the more variable background, which yields higher noise levels in the MOPEX extraction, and partly due to the fraction of 8.0 μm sources ($\sim 5\%$) that is extracted by the less accurate aperture photometry method (see Sec. 2.2.4), instead of by the profile fitting method. Most of the sources extracted by this method have a relative flux uncertainty of 10% (see Sec. 2.2.4), which yields a magnitude uncertainty of ~ 0.1 . Occasionally, the background determination in the aperture photometry method is very uncertain, which is the reason for introducing a relative flux error of 50%, resulting in a magnitude uncertainty of ~ 0.5 .

The same holds for the MIPS 24 μm sources, nearly half of which are extracted by the less accurate aperture photometry method. The median magnitude uncertainty for MIPS is 0.05. Two of the twenty MIPS sources have an uncertainty in the magnitude of ~ 0.5 (see also Fig. 6), resulting from very uncertain background determination in the aperture photometry method. The other seven MIPS sources extracted by this method have a magnitude uncertainty of 0.1. As is seen in Fig. 6, the remaining MIPS sources, extracted by MOPEX, have magnitude uncertainties below 0.06.

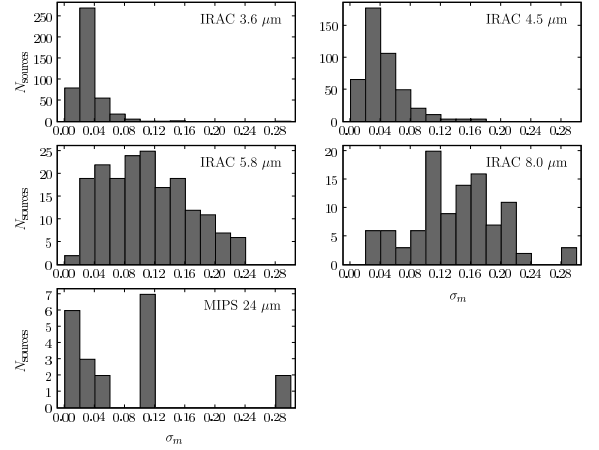


Fig. 6. Distribution of the magnitude uncertainties, as calculated in Eq. 5, of all sources present in table 4 on page 29. The last bin contains all values larger than 0.28; for example, all the uncertainties of 0.5 in IRAC 8.0 μm and MIPS end up in this bin.

2.5. Band merging

The point source extraction described in previous sections results in lists of sources with sky coordinates and a magnitude in only one band. The evolutionary state and physical conditions in YSOs are reflected in the color. A color of an object can only be defined if there are at least two fluxes in different wavelength bands associated to the object (see also Sec. 5.1). In addition, for the SED analysis performed in Sec. 5.2, one needs at least three fluxes associated to one source. It is therefore necessary to merge the point source lists from individual bands in order to obtain a list of sources with magnitudes in as many of the five bands as possible.

2.5.1. Matching bands by position

The band merging is done by associating a source in one band (the ‘reference band’) to sources in other bands. For every source in the reference band, matches are defined as sources in other bands that fall within a certain area centered around the reference source. This area is circular and has a radius determined by the quadratic mean of two position uncertainties: that of the reference source and that of the source being considered for matching. This radius is fixed to half the size of an IRAC pixel (i.e. 0.6'') if it drops below this value. If one or more matches are identified for a reference source, it is copied to a table listing its sky position and its magnitudes and uncertainties in now at least two bands. In addition, the table contains a number representing an average position uncertainty for every entry, calculated by the squared mean of the matching distances.

To eliminate much of the effects of bias due to the arbitrary starting point (the reference source), the band merging is done three times, each with a different set of reference sources: all sources from IRAC 4.5, from IRAC 8.0 and from MIPS 24.

2.5.2. Filtering the list

The combination of these three band merging runs obviously results in a highly redundant source list. The list is filtered for duplicates and redundancies in four steps.

Table 3. Magnitudes of the faintest and brightest sources in the merged list (table 4 on page 29).

band	faintest source	brightest source
IRAC 3.6 μm	16.0	8.5
IRAC 4.5 μm	14.8	7.6
IRAC 5.8 μm	11.8	7.0
IRAC 8.0 μm	11.3	6.6
MIPS 24 μm	9.3	4.4

Identical matches are to be expected: a robust merging routine will in most cases match the same sources to each other regardless which of these sources is chosen as the reference source. It is therefore reassuring that identical matches are indeed found while cross-checking the three lists originating from the different choices for the reference band. Nonetheless, duplicate entries are not desirable in the final list, so they are removed in the first filtering step. The same holds for entries containing the same but less information compared to another entry⁶ (step 2).

In the third step, matches are considered where one source is successively matched to > 1 source in a particular other band. These cases are disentangled by selecting the match with the smallest average distance and removing the rest.⁷

The last filtering step detects sets of entries containing complementary data. For example, one entry may contain magnitudes for bands I, II, III and IV while another entry contains magnitudes for bands II, III and V. If the coinciding bands (II and III) list identical information, then the two entries are merged into one new entry containing magnitudes for all five bands.

2.5.3. Merged list

Starting from three lists of reference sources (almost 600 in IRAC 4.5, about 100 in IRAC 8.0 and 20 in MIPS 24), matching to sources in other bands and applying the filtering as described above, the end result is a list of 490 sources. These include 27 non-matched entries: 20 only have a magnitude in IRAC 8.0 and seven only have a magnitude in MIPS 24. Objects that only appear at 8 or 24 μm are interesting when looking for young stellar objects: they show emission at a particular long wavelength, but none (or not detectable) at the shorter wavelengths. These entries are deliberately retained in the final list for possible further study.

A total of 54 objects have magnitudes in all four IRAC bands. Only five of these also have magnitudes in MIPS 24 μm .

The magnitudes of the brightest and faintest sources in the merged list (cf. the limits in table 2) are given in table 3. In IRAC 8.0 μm , the faintest source in table 3 (magnitude 11.3) is extracted by aperture photometry and is therefore not present in table 2. The faintest source in the MIPS band (9.3), also extracted by aperture photometry, is two magnitudes fainter than the faintest MIPS source extracted by MOPEX (see table 2).

⁶ For example: if entry *A* lists magnitudes in all five bands, while entry *B* contains the same magnitudes in the first three bands and none in the last two, entry *B* is removed.

⁷ For example: source *a* from band II is matched to source *k* from band I, but also to sources *m* and *n* from band I. Out of these three, the match with the smallest average distance is selected and the other matches are removed from the list.

2.6. Final source list

The final sourcelist, bandmerged by the method described in Sec. 2.5, is presented in table 4, from page 29 onward. Position uncertainties are not explicitly listed per source. They are generally $\sim 0.5''$ and never above $2''$.

3. Comparison to IRAC sources from GLIMPSE

The Galactic Legacy Infrared Mid-Plane Survey Extraordinaire (GLIMPSE), one of the Spitzer legacy science programs, observed much of the galactic plane between $b = -1^\circ$ and $+1^\circ$ with the IRAC instrument. This survey includes the coordinates of IRDC G48 ($\ell = 48:6$, $b = -0:3$), which provides an opportunity to compare the point source lists from Section 2.2.2 to the GLIMPSE archive (see Benjamin et al. (2003) and the project webpage⁸). The archive is used as a benchmark to validate the source extraction described in the previous chapter. In fact, this validation has been used in an iterative process, intertwined with the point source extraction described in Chapter 2, to provide a better understanding of the methods and obtain more consistent results.

3.1. Properties of GLIMPSE

The GLIMPSE survey, with a total exposure time of 2.4 seconds at every position, has detection limits of 0.2, 0.2, 0.4 and 0.4 mJy for the four IRAC bands in order of increasing wavelength. These limits hold for a uniform background level and are expected to increase as the background level becomes more difficult to determine. In the field corresponding to our observations, the dimmest sources in the first two bands are indeed ~ 0.2 mJy. In the 5.8 and 8.0 μm bands, however, the dimmest sources in the relevant part of the archive are 0.8 and 0.6 mJy, respectively. In the images of G48, the level as well as the variability of the diffuse background radiation increases from 3 to 8 μm . At the higher wavelengths, this makes it more difficult to detect sources close to the detection limit for the ideal case of a flat background.

The GLIMPSE archive lists a photometric uncertainty of typically < 0.3 magnitudes. The position uncertainties in the archive are $0.3''$.

The photometry by GLIMPSE uses standard DAOPHOT routines, some of which are adapted to fit the specific needs of crowded mid-infrared fields with highly variable background. The routines perform variable background estimation, iterative point source function fitting and source removal.⁹ The GLIMPSE archive includes all sources extracted at a 3σ detection limit above the local background.

3.2. Comparison to our data

The portion of the GLIMPSE archive used here is of the same part of the sky as our observations, recorded by the same instrument on board the same telescope. The main differences between the two sets of fluxes being compared in this chapter, are (i) the methods used to extract sources from the images and (ii) the total exposure time.

The point source extraction method employed in GLIMPSE is summarized in Sec. 3.1. Our point source extraction is described in detail in sections 2.2.2 - 2.2.4. The flux and magnitude calibration and uncertainties are discussed in sections 2.3 and 2.4.

⁸ <http://www.astro.wisc.edu/glimpse/>

⁹ See the point source photometry document and the quality assurance document at <http://www.astro.wisc.edu/glimpse/docs.html> for a more detailed description of the GLIMPSE point source extraction.

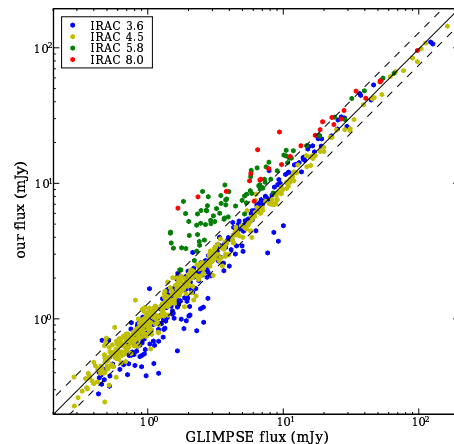


Fig. 7. Comparison of fluxes from the GLIMPSE archive against ours. Every colored dot represents a source that is extracted from our images at a position close to an entry in the GLIMPSE archive (see text). The solid line indicates the one-to-one relation; the dashed lines indicate the boundaries of the 0.3 magnitude uncertainty region of the GLIMPSE archive.

The longer exposures time allows for the use of the high dynamic range mode (see Sec. 2.1) and a dithering pattern on sub-pixel scales. This is expected to provide superior initial conditions for the point source extraction in terms of point source fitting accuracy and background noise.

Although our observations are much deeper (see Section 2.1), the faintest sources detected in our images are not below the detection limits of GLIMPSE. Our position uncertainties are also of the same order as those in the GLIMPSE archive. The photometric uncertainty however is significantly less for our sources: generally < 0.1 magnitude in IRAC 3.6 μm and 4.5 μm and < 0.22 for the other two IRAC bands, as described in Sec. 2.4. This is primarily due to the longer (over a factor of 40) total exposure time, which allows for more accurate background determination and point source fitting.

Using a method similar to that used in Section 2.5 for the band merging, the sources from our four IRAC lists are matched to sources in the same band in the MIPS archive, based on sky position. Starting from a particular GLIMPSE source, every source in our lists that falls within two times the position uncertainty of that GLIMPSE entry is considered to be the same source. If there are two or more possible matches, the one closest in position is chosen. The fluxes of all sources matched to one in the archive are plotted in Fig. 7 for the four IRAC bands.

The GLIMPSE detections that do not match in position to any of our sources are primarily located near the edges of our field, where the coverage of the observations is less. In addition, the majority of these GLIMPSE sources are below 1 mJy for the 3.6 μm and 4.5 μm bands and below 2 mJy for the 5.8 μm and 8.0 μm bands. These sources are difficult to detect with respect to brighter sources. They are therefore expected to have larger position uncertainties, which is a possible cause for mismatching.

According to the GLIMPSE Quality Assurance Document, their reliability criterion of $\leq 0.5\%$ false detections is achieved at 0.6 mJy, 0.4 mJy, 2 mJy and 10 mJy for IRAC 3.6 μm , 4.5 μm ,

5.8 μm and 8.0 μm , respectively.¹⁰ The majority of the matches in the first two bands fall within the uncertainty limits indicated by the dashed lines in Fig. 7, especially at higher fluxes, where GLIMPSE's reliability is at its highest.

Both the 5.8 μm sources and the 8.0 μm sources seem to be systematically overestimated at fluxes < 8 mJy (or underestimated by GLIMPSE), although they do show a fairly good match at higher fluxes (cf. the reliability thresholds at 2 mJy and 10 mJy, respectively). The trend seen in the 5.8 μm and 8.0 μm points in Fig. 7 is consistent with a constant offset of 3-6 mJy between GLIMPSE fluxes and ours. A constant offset added to a straight line will appear as a deviation from constant slope in the low-flux regime of log-log space (see Fig. 7). At higher fluxes, in the regime where the offset is negligible with respect to the original value, the shift in the relation will hardly be noticeable.

To confirm this, a linear regression fit is performed on the points shown in Fig. 7. The four resulting straight lines ($y = ax + b$) have a slope (a) ranging between 0.93 and 1.06. The offsets (b) are 0.16 and 0.09 mJy for IRAC 3.6 μm and IRAC 4.5 μm , respectively. Those of IRAC 5.8 μm and IRAC 8.0 μm are larger: 3.1 and 6.8 mJy.

3.3. Fixing the discrepancy

The constant offset in the linear relation found above could be explained by either a systematic overestimation of the background emission by GLIMPSE, or a systematic underestimation of the background by our method. There is no evident sign of either.

As is stated in the GLIMPSE data product description, the uncertainties in the archive are generally larger for the 5.8 μm and 8.0 μm band than at the shorter wavelengths, due to higher background. This effect can be expected to be particularly strong in a region such as G48, where the background radiation does not only have a high level, but is also highly variable over the field. This is to stress that the discrepancy seen in these two bands could be due to systematic effects in the GLIMPSE extraction method, in our method, or possibly in both.

The discrepancy in the two highest wavelength bands of IRAC is recognized, but we choose to trust the extraction method from Sec. 2.2.2. If the fluxes would be 'corrected' to match the GLIMPSE fluxes, by susubtracting the offset values found in Sec. 3.2, the 5.8 μm and 8.0 μm fluxes would be shifted downward.

The effect of this would be most notable in the dimmer sources, where the relative flux correction is largest. If the magnitudes $[5.8] \gtrsim 9$ and/or $[8.0] \gtrsim 8$, the correction would have an effect of > 0.1 magnitude. For example in source S14 ($[5.8] = 10.54$, $[8.0] = 9.01$, see Table 4), the 'corrected' 5.8 and 8.0 μm fluxes would be roughly half of what they are now. However, since *both* 5.8 and 8.0 μm fluxes are effectively divided by two, the $[5.8] - [8.0]$ would hardly change for this source. Generally, since the shift is larger for the 8.0 μm fluxes, the $[5.8] - [8.0]$ color would shift to the left (towards the blue) by some tenths of magnitudes for most of the fainter sources. This is a significant shift with respect to the magnitude uncertainties which are generally $\lesssim 0.2$ magnitude.

With respect to the SED model fitting (see Sec. 5.2), it is noted that the fits to the sources that would suffer from a flux correction (S8, S13 and S14), the models have difficulties explaining the relatively large fluxes in IRAC 5.8 μm and 8.0 μm .

In these cases, the quality of the fits of model SEDs to the data-points might even improve after a flux correction in these two bands (cf. Figs. 24 and 23).

¹⁰ Maximum reliability ($\leq 0.1\%$ false detections) for 5.8 μm is reached only above 10 mJy and for 8.0 μm above 20 mJy.

4. YSO models

The physical and chemical parameters and processes that play a role in specific YSOs are best explored by comparing the data points (fluxes at various wavelengths) to models of YSOs. The most detailed way to consider an object is by examining its complete spectral energy distribution (SED). Robitaille et al. (2006) provide a set of such models.

First, a description of the models and some advantages and caveats are given in this chapter. In Chapter 5, two methods for classifying the stellar content of the cloud are employed. The loci of sources in color-color space are examined and compared to the spread of YSO models in the same color-color space in Sec. 5.1. In Sec. 5.2, the data points of a number of sources are fitted to a grid of model SEDs; the best-fit model is then used to derive physical parameters for the observed object.

The observations are regarded as the starting point from which to analyze the young stellar content of the IRDC. The set of YSO models described in Sec. 4.1 is based on an accepted mode of star formation and various parameters are sampled within accepted ranges to account for different conditions and evolutionary stages.

Of course, the crucial assumption is that all data compared to the model is in fact originating from young, embedded stellar objects. In the SED fitting (Sec. 5.2), this assumption is validated by fitting every observed source not only to the YSO model grid, but also to a set of stellar photosphere SEDs. A source is only classified as a YSO as long as the photosphere is not a better fit to the data than the YSO SED.

Additional objects, other than YSOs, that may show color indices and SED properties similar to those of YSOs can be present in our field. The probability of finding such objects is discussed in Sec. 6.1.

4.1. The YSO model grid

The set of YSO models presented by Robitaille et al. (2006) is obtained by running a numerical Monte Carlo radiation transfer code. The goal is to combine all theoretical knowledge and observational evidence of YSO physics into one grid of YSO models. Different environments and star formation ‘modes’ are taken into account by using a large spread in the input parameters (e.g. the input stellar mass ranges from 0.1 to 50 M_{\odot}).

All geometry is assumed to be axisymmetric. In general the system consists of three components:

- A central luminosity source, i.e. the protostar;
- A rotationally flattened infalling envelope with bipolar cavities;
- A flared accretion disk.

Of each of these components, a number of physical parameters is sampled over ranges constrained by previous theories and observations. These input parameters for the code are listed per component in Table 5. The environment of the YSO can be viewed as a fourth component, since it directly influences the envelope through the ambient density (outside the envelope). In addition, the observed energy distribution is affected by interstellar extinction, parameterized by A_V . The disk inner radius, $R_{\text{disk}}^{\text{min}}$, is always set to the same value as the envelope inner radius. Other parameters, such as the age of the central source, are derived from the sampled parameters.

The resulting SEDs are convolved with broadband filters of IRAC and MIPS, with the J, H and K bands, SCUBA filters, and many more. With this method, the fluxes and magnitudes

Table 5. Input parameters for the model grid in Robitaille et al. (2006). Note that the viewing angle ϕ is not an input parameter for the radiative transfer code, it is only used to determine how much of every component is visible for the observer.

Central star parameters		Envelope parameters	
Symbol	Description	Symbol	Description
M_{\star}	Stellar mass	\dot{M}_{env}	Envelope accretion rate
R_{\star}	Stellar radius	$R_{\text{env}}^{\text{max}}$	Envelope outer radius
T_{\star}	Stellar temperature	ρ_{cavity}	Cavity density
		θ_{cavity}	Cavity opening angle

Disk parameters		Other parameters	
Symbol	Description	Symbol	Description
M_{disk}	Disk mass (gas+dust)	ρ_{ambient}	Ambient density
$R_{\text{disk}}^{\text{max}}$	Disk outer radius	ϕ	Viewing angle
$R_{\text{disk}}^{\text{min}}$	Disk inner radius		
\dot{M}_{disk}	Disk accretion rate		
z_{factor}	Disk scaleheight factor		
β	Disk flaring angle		

of every model can be determined in every band, which gives the opportunity of comparing *observed* magnitudes and colors to those of the model grid.

4.1.1. Advantages

The primary modeling goal of Robitaille et al. (2006) is to model and fit mid-IR emission of YSOs. Moreover, their code is developed bearing in mind the specific goal of applying the model grid to archives of Spitzer Space Telescope data, such as those of GLIMPSE (IRAC instrument) and MIPS GAL (MIPS instrument). This makes their model grid particularly useful for the interpretation of our data.

The advantage of the Monte Carlo code is that every photon that ends up contributing to the total SED can be traced back to its last point of origin. This allows for the possibility to examine in detail, per specific model, which of the components provide the largest contributions to the total SED at particular wavelengths.

It is advantageous to use a pre-defined set (or grid) of models. This allows for general classification of objects and at the same time it prevents ‘overinterpretation’ of the data, because it is immediately clear how much variation can exist in observed properties of a particular model or stage (see Fig. 8).

4.1.2. Caveats

While using this model grid to assess young stellar content of the G48 region, the general caveats listed here must be kept in mind.

- No PAH or small-grain continuum emission is included in the models. This results in an underestimate of the mid-IR flux.
- The total luminosity generally decreases with time, so there is some bias towards the younger evolutionary stages, since they are simply brighter. Especially in a fairly distant region such as IRDC G48, at ~ 2.5 kpc, one must keep in mind that later stages and intrinsically fainter sources are less likely to be observed.
- Robitaille et al. (2006) are confident that the grid is adequate for a large range of YSO parameters, *except* for sources with $L < 0.2 L_{\odot}$ or in very dense clusters of more than 1000 stars pc^{-3} .

Table 6. YSO evolutionary stages as defined by Robitaille et al. (2006). Note that the threshold values are defined in terms of the mass of the protostar, M_* .

Stage	components	M_{disk}/M_*	\dot{M}_{env}/M_*
0, I	accreting envelope	any	$> 10^{-6} \text{ yr}^{-1}$
II	disk, remains of envelope	$> 10^{-6}$	$< 10^{-6} \text{ yr}^{-1}$
III	optically thin disk	$< 10^{-6}$	$< 10^{-6} \text{ yr}^{-1}$

- The sampling of the parameters (see Table 5) is sparse (Thomas, priv. comm.). There is the intention to improve this in the future, at the cost of more computing power.
- No heating by the external interstellar radiation field is included. This may impact especially very low-luminosity sources (Young et al. 2004).

In addition to the above caveats, the following properties of the model grid affect especially high-mass YSOs. They may not be modeled correctly due to these imperfections of the models.

- Puffed up disks due to photoionization-driven winds may exist around very luminous young stars, this is not incorporated in the models.
- Optically thick *gas* may be present in large dust holes, this is not explicitly accounted for in these models. On the other hand, this does make every resulting SED scalable to the gas-to-dust ratio, which is assumed to be 100 in these models.
- Different geometries may be necessary to account for forming star clusters inside a single envelope. However, it is argued that clustered star formation has the most significant effect on the SED primarily through a larger hole in the center of the disk and envelope. Large inner holes are explicitly allowed for in the input values to the code.

4.2. Stage classification

Robitaille et al. (2006) propose a new classification scheme for YSOs, which are called ‘Stages’, as a replacement for the classically used ‘Class’ scheme (see Sec. 1.2). It is correctly argued that the Class scheme is based purely on an observational parameter: the slope of the mid-IR SED.

Instead, the ‘Stage’ scheme classifies YSOs by their actual evolutionary state, meaning that a Stage I object is always in an earlier phase of evolution than a Stage II source, which is always in an earlier phase than a Stage III source. The evolutionary track is considered to be the accepted track where, once the protostar has switched on, there is still a lot of circumstellar material present. This forms the envelope, in which bipolar cavities are formed due to outflow jets from the central source, which is unable to dissipate sufficient energy at other angles. This phase is called ‘Stage I’ by Robitaille et al. (2006) (see Table 6). In the subsequent phase (‘Stage II’, the classical T-Tauri phase), most of the envelope accretion dies out and the central star and the circumstellar disk – which have been hidden underneath the in-falling envelope until now – become visible. In the final phase, ‘Stage III’, even the accretion disk becomes largely optically thin and more and more of the central source becomes directly visible.

Although it is generally true – also in the scheme of Stages proposed by Robitaille et al. (2006) – that the mid-IR SED changes from rising (high envelope emission longwards of 20 μm) to flat (declining envelope, more disk radiation) to falling (optically thin disk, more flux directly from the photosphere),

various other parameters besides the actual evolutionary state affect the SED. This results in ambiguities in the Class scheme: e.g. a Class II object is not always in a later phase of evolution than a Class I object.

The ‘Stage’ classification scheme for YSOs is used in the analysis in Chapter 5.

5. Analysis and results

5.1. Color-color diagrams

As is shown in Fig. 9, color-color diagrams using the four IRAC bands and the MIPS 24 μm band can be used in an attempt to separate the various ‘stages’ of evolution from Table 6. All 54 sources in our sample for which a magnitude can be calculated in each of the four IRAC bands are shown in IRAC color-color space in Fig. 10. The difference between the magnitudes in the first two IRAC bands is plotted along the vertical axis, and the difference between the other two IRAC bands is plotted along the horizontal axis.

Note that all color-color diagrams in this thesis use color indices defined such that a higher value of the index always means a redder color. This means that in all diagrams, red is always to the top and to the right and blue is always to the bottom and to the left.

5.1.1. Stage I objects

There are sixteen sources that fall within (or above) the Stage I region in Fig. 10. All these are marked in the top panel of Fig. 11 by their names to the top right of the source position. The name of each source refers to the corresponding entry in Table 4. Both S17 (at $([5.8] - [8.0]; [3.6] - [4.5]) = (0.04; 2.34)$) and S55 $(-0.29; 3.10)$ lie above the Stage I region¹¹ indicated in Fig. 9, i.e.: they show extremely red colors in $[3.6] - [4.5]$, but hardly any relative excess in $[5.8] - [8.0]$. Judging from the spread of Stage I candidate objects in the top panel of Fig. 11, there does not seem to be a preference for the youngest sources to lie closer to the dark cloud filament.

Of these Stage I candidates, S114 at $(-0.75, 0.21)$ in IRAC color-color space, S5 (1.70, 1.13), S55 and S110 (0.08, 1.52) are among the candidates where the least confusion with stellar photospheres (around (0, 0) in IRAC color-color space) or later YSO stages (bottom right part of the color-color diagram) is possible. Based on the facts that these four objects show colors consistent with a very early star forming phase *and* have positions on the sky close to the dense filament. The combination of these two

¹¹ Source S93 also lies above this region, it has a $[3.6] - [4.5]$ color of ~ 7 , but has a very large uncertainty in $[3.6]$, and is the faintest source in the list at 3.6 μm . This source is therefore not considered in the analysis.

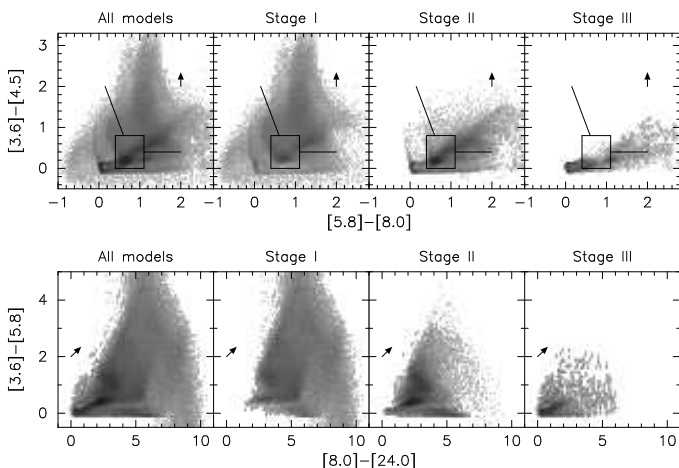


Fig. 8. The spread of models in IRAC and IRAC+MIPS color-color space from Robitaille et al. (2006).

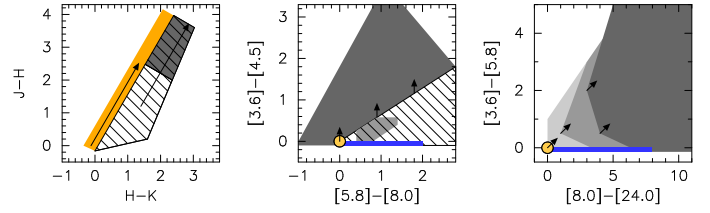


Fig. 9. JHK, IRAC and IRAC+MIPS color-color diagrams showing the spread of the models of the three evolutionary stages in Robitaille et al. (2006). From dark to light gray: the regions where most models are Stage I, Stage II and Stage III, respectively. The hashed region in the IRAC color-color space indicates a region where models of all three stages can be found. The yellow disks indicate the loci of stellar photospheres in the absence of extinction. The reddening vectors (arrows) show an extinction of $A_V = 20$. In the blue rectangular areas, only disks with large inner holes are expected. This figure is part of Fig. 23 from Robitaille et al. (2006).

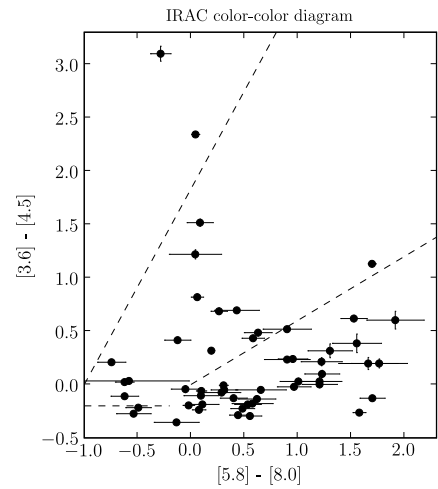


Fig. 10. IRAC color-color diagram, showing all 54 sources of which magnitudes are known in all four IRAC bands. The dashed lines indicate the approximate ‘Stage I region’ from Robitaille et al. (2006), see Fig. 9.

conditions makes the above mentioned four sources the most likely candidates to be very young stars associated to the IRDC.

5.1.2. Disk objects

Further towards the right of the color-color diagram are sources which are less likely to be Stage I objects, although Fig. 8 and 9 do show that YSO models of any stage can be found in this region of the IRAC color-color diagram.

Any disk objects (Stage II or III) are to be found in this bottom right region. A total of 38 objects can be found in our sample in this color regime. The sky locations of these ‘possible disk objects’ are shown in the bottom panel of Fig. 11. None of these lie as far into the extinction cloud as the four probable Stage I sources from Sec. 5.1.1. Perhaps the exceptions are S57 and S75, but even these two do not appear to be in regions that are as heavily extinguished as those of S114, S5, S55 and S110, the probable Stage I candidates.

5.1.3. Possible photospheres

Photospheres, in the absence of extinction, are expected to fall in the region close to (0,0) in the IRAC color-color diagram (the

Possible photospheres

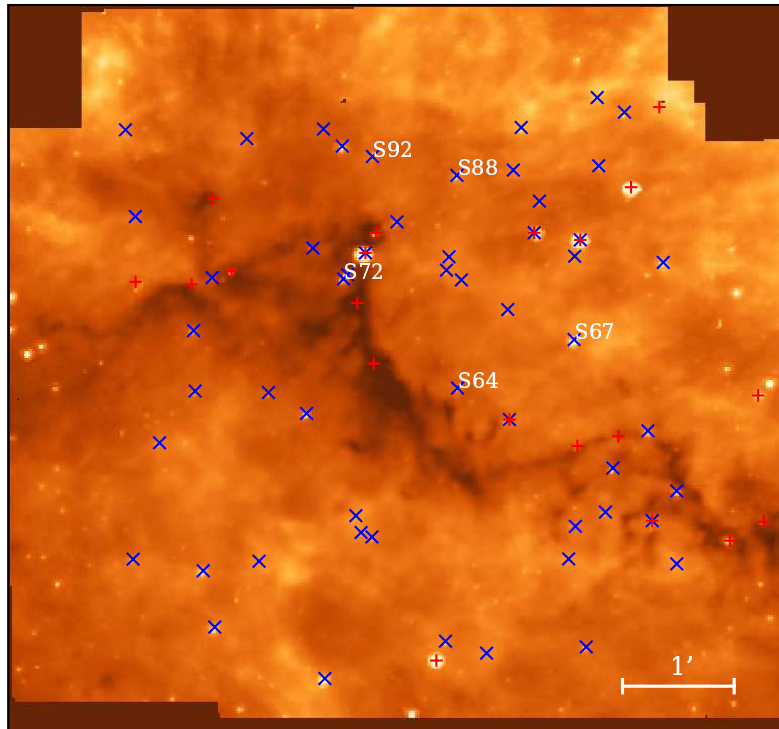


Fig. 12. The sky positions of possible photospheres (both colors between 0.2 and -0.2) are indicated by the names of the sources. Blue crosses and red plusses mean the same as in Fig. 11.

yellow disk in Fig. 8). If the region is conservatively defined as the square where both color indices lie between -0.2 and 0.2 , there are five objects classified to be a possible photosphere. The sky positions of these sources are marked in Fig. 12.

The most probable candidates for photospheres, not physically connected to the infrared dark cloud, are foreground sources along the line of sight toward the cloud. On the red side of the $(0, 0)$ locus, one could expect reddened photospheres. The objects closest in color are in this case S18 ($0.19, 0.32$) and S113 ($-0.13, 0.42$). But for photospheres to be shifted upwards along the reddening vector (see Fig. 9) to $[3.6] - [4.5]$ colors in the order of 0.4 , the visual extinction should be of the order of 40 . In addition, S18 is also visible at $24 \mu\text{m}$, which makes it highly unlikely to be a photosphere, even if extincted.

5.1.4. Blue objects in $[3.6] - [4.5]$

At the bottom of the color-color diagram in Fig. 10, quite a number of objects appear with a negative $[3.6] - [4.5]$ color, in a region where density of models from the model grid is low (see Fig. 8). This can be due to scattering of stellar light in the cavity, see for example the SED fit to IRAS 04368+2557 in Robitaille et al. (2007). Alternatively, emission from PAH molecules can be a cause for blue colors in $[3.6] - [4.5]$ and at the same time red colors in $[5.8] - [8.0]$. In the current set of models, PAH emission is not included; it will be in future versions (Thomas Robitaille, priv. comm.).

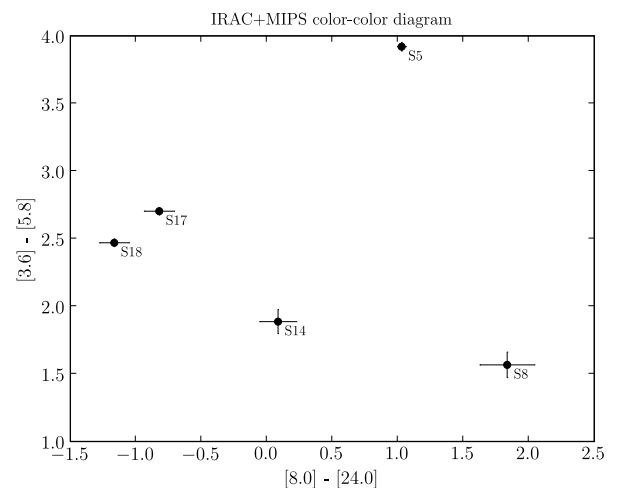


Fig. 13. IRAC+MIPS color-color diagram, showing the 5 sources of which magnitudes are known in the required IRAC bands and in MIPS $24 \mu\text{m}$.

5.1.5. IRAC+MIPS colors

There are five sources in the field for which fluxes are extracted in all four IRAC bands *and* in MIPS $24 \mu\text{m}$: S5, S8, S14, S17 and S18. In Fig. 11, these have both a blue cross and a red plus sign. Fig. 13 shows the distribution of these objects in $[3.6] - [5.8] / [8.0] - [24]$ color-color space. Object S8, which was marked as a

possible disk source in Sec. 5.1.2, is confirmed to be on the edge of the Stage II and Stage III regions shown in the right panel of Fig. 9.

The other four objects show very blue $[8.0] - [24]$ colors, such that they fall completely outside of the color range of the models shown in the bottom panel of Fig. 8. This can be due to the extinction feature¹² at $8 \mu\text{m}$, which may be strong relative to the extinction around $20 \mu\text{m}$ in some cases. The $[8.0] - [24]$ colors have been checked against those of AGB models and observations (data from Groenewegen (2006), see also Sec. 6.1.1). AGB colors never fall blueward of $[8.0] - [24] = 0$, but rather in the same color ranges as the YSO models presented earlier in this chapter.

The conclusion for S17 and S18 – and for S14 to some extent – is that they are unlikely to be embedded YSOs or AGBs.

5.2. SED fitting

Assessing objects by color indices, as is done in the previous section, places the strict requirement that for every source, magnitudes must be known in each of the required band, e.g. all four IRAC bands if one desires to make a diagram such as Fig. 10. This requirement can be made less strict when the possibility is offered to fit an SED to any number of data points.

For example, when a particular object has associated fluxes in the near-IR J-band, two IRAC bands, one MIPS band and perhaps an upper limit in sub-millimeter observations, it is impossible to place it in any of the traditional color-color diagrams. The first advantage of an SED fitting method is that, although there is not data in *all* standard near- and mid-IR bands, the available data points can still be inspected in order to extract information about the (partial) shape of the SED, and therefore about the physical parameters that give rise to such an SED. The second advantage is that one can use all available information per source *at once*. There is no need for a restriction to only near-IR colors or to only mid-IR colors: for each source, one can use all data that is available.

Compared to a color-color diagram analysis, with this more detailed method of examining objects one can find not just a single range of parameters that can explain all observed sources in a particular field at once, but rather for each individual source a possibly more constrained set of parameters than can explain the observed SED.

The really interesting sources from our point of view shine brightly at $24 \mu\text{m}$ and lie tightly around the extinction filament that is called the infrared dark cloud. The positions of all twenty objects with a MIPS magnitude are shown with their names in Fig. 14. At least half of these sources – if not three quarters – appear to be spatially associated to the dark cloud filament. The extinction at these loci is so strong, that often nothing of the central source can be seen at shorter wavelengths ($3.6, 4.5 \mu\text{m}$). Of course, the fitting tool will be able to provide better, more constrained results when more observed fluxes in different wavelength bands are provided. However, a model fit can be attempted with as little as three data points.

After a description of the fitting tool in Sec. 5.2.1, all sources that have a MIPS $24 \mu\text{m}$ flux and fluxes in at least two other bands are individually discussed in Sec. 5.2.2 and 5.2.3. The approach of considering only sources that have a flux in MIPS $24 \mu\text{m}$ is taken, because fitting SEDs to datapoints only in the IRAC regime ($3-9 \mu\text{m}$) generally results in very degenerate sets of model SEDs, all fitting the data points with little spread in χ^2 .

¹² PAH related? PAHs are not incorporated in these models...

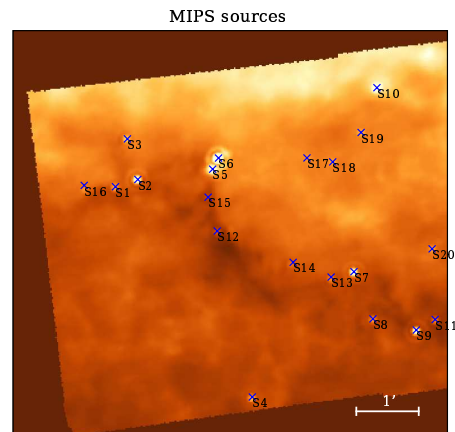


Fig. 14. All twenty sources for which a MIPS $24 \mu\text{m}$ magnitude is known, overlaid on the MIPS $24 \mu\text{m}$ mosaic.

This becomes clear from experience with fitting different sets of datapoints to the SED model grid. It is also noted by Robitaille et al. (2006, 2007) that additional data at longer wavelengths (e.g. MIPS $24 \mu\text{m}$) is crucial in making a clear distinction between YSO SEDs with varying parameters.

5.2.1. SED fitting tool

An SED fitting tool (Robitaille et al. 2007) is available as a downloadable command line program or an online fitting tool¹³. The tool uses the pre-computed grid of models from Robitaille et al. (2006) and expects user input in the form of at least three data points, each of which should list (i) in which of the bandpasses the flux was measured¹⁴, (ii) a flux (or a magnitude), (iii) an uncertainty in the flux (or in the magnitude) and (iv) the aperture used in the flux measurement. Upper limits in certain bands may also be specified, but are not counted as real datapoints in setting the minimum amount of three datapoints. For example, the values in Table 7 can be entered directly into the model fitter to get an SED fit, but it would not be sufficient to provide fluxes in just two bands and an upper limit in a third band. In addition, the user is asked to specify a distance range (d_{\min}, d_{\max}) and a range in visual extinction, A_V . Finally, there is an option to specify whether any of the apertures are smaller than the apparent extent of the source, i.e. whether the source is resolved.

The SEDs from the model grid (see Sec. 4) are convolved with common filter bandpasses. The convolved fluxes are subsequently interpolated with respect to the user specified apertures. A number of distances between d_{\min} and d_{\max} is sampled in order to scale the convolved, interpolated model flux. A second scaling is applied to account for extinction, using an extinction law derived by Indebetouw et al. (2005) and leaving the extinction at the reference wavelength (A_V) as a free parameter. A pattern $P_v(\lambda_i)$ is defined in terms of the convolved (passband), interpolated (aperture) and scaled (distance) model fluxes $M_v(\lambda_i)$ and

¹³ <http://caravan.astro.wisc.edu/protostars/>

¹⁴ At the time of writing, twenty filters are already available between 1 and $900 \mu\text{m}$, including all 2MASS, Spitzer, IRAS, MSX and SCUBA filters. More filters can be requested by users. A separate version of the fitting tool even accepts flux values at arbitrary wavelength; this is not used in this thesis.

the extinction parameters κ_{λ_i} and κ_V provided by Indebetouw et al. (2005):

$$\log_{10}(P_v(\lambda_i)) = \log_{10}(M_v(\lambda_i)) - 0.4A_V \frac{\kappa_{\lambda_i}}{\kappa_V}. \quad (6)$$

It is this pattern from Eq. 6 that is fitted to the data points, $F(\lambda_i)$ at wavelengths λ_i , specified by the user. For every SED in the model grid and for a number of distances between d_{\min} and d_{\max} , a χ^2 per datapoint (i.e. it is divided by the number of datapoints N) is calculated through:

$$\chi^2/N = \frac{1}{N} \sum_{i=1}^N \left(\frac{(\log_{10}(F_v(\lambda_i))) - \log_{10}(P_v(\lambda_i))}{\sigma(\log_{10}(F_v(\lambda_i)))} \right)^2, \quad (7)$$

where the σ factor in the denominator is the square root of the ‘unbiased’ flux variance in \log_{10} space, which is related to the relative flux uncertainty in each data point supplied by the user. Note that the definition of χ^2/N in Eq. 7 differs from the usual χ^2 definition by a factor N . The ‘ χ^2 per datapoint’ defined in Robitaille et al. (2007) is equivalent to χ^2/N in this thesis.

The best fit is considered to be the SED that results in the minimal value of χ^2 for the given set of datapoints. Intercomparison of χ^2 values between sources is not meaningful, since neither χ^2 nor χ^2/N are actual independent measures of the ‘goodness of fit’. As Eq. 7 shows, χ^2 decreases as the uncertainty in the measured datapoints (σ) increases. Therefore, a low absolute value of χ^2 for a particular source does not necessarily indicate a good fit, it is merely a method for determining the best fit for a given set of datapoints and uncertainties.

In addition to a comparison of the datapoints to the model YSO SEDs, the same datapoints are fit to stellar photosphere SEDs with effective temperatures ranging from 2000 to 50 000 K. This feature is implemented in order to assess whether the same object might be explained by a normal stellar photosphere instead of a YSO model. Input to the model fitter of only magnitude 0 values (a standard Vega-like object) in a number of bands ranging from optical to the 24 μm MIPS band indeed fits significantly better to a stellar photosphere than to an SED model.

5.2.2. Brightest cores

The two brightest sources at 24 μm , S5 and S6, lie very close to the emission peak ‘P1’ identified by Ormel et al. (2005) in SCUBA images at 450 and 850 μm . In fact, the position of P1 falls almost exactly between our S5 and S6. At SCUBA resolution (the 850 μm beam has a FWHM in the order of 20'', the 450 μm beam is roughly half as wide), P1 appears as one peak, albeit with a slightly elongated shape, see Fig. 15. With Spitzer resolution ($\sim 6''$ at 24 μm and $\sim 2''$ at 8 μm), it is now evident that there are at least two distinct sources at this position. The cores S5 and S6 both lie well within the cut-off radius of 55'' used for P1 in Ormel et al. (2005).

S6

The brightest source at 24 μm is S6; it has no associated flux at either 3.6 or 8.0 μm , but there are fluxes known at 4.5 and 5.8 μm . Three data points are the minimum amount required by the SED fitting tool from Robitaille et al. (2007). The resulting model fits are shown in Fig. 16. All models are shown that have a χ^2/N not in excess of the χ^2/N of the best fitting model +3. It is clear that many different models can fit the same three data points within almost the same deviation. This results in many degeneracies in the physical parameters that determine the properties of each ‘fitting’ SED. For example, according to these fits,

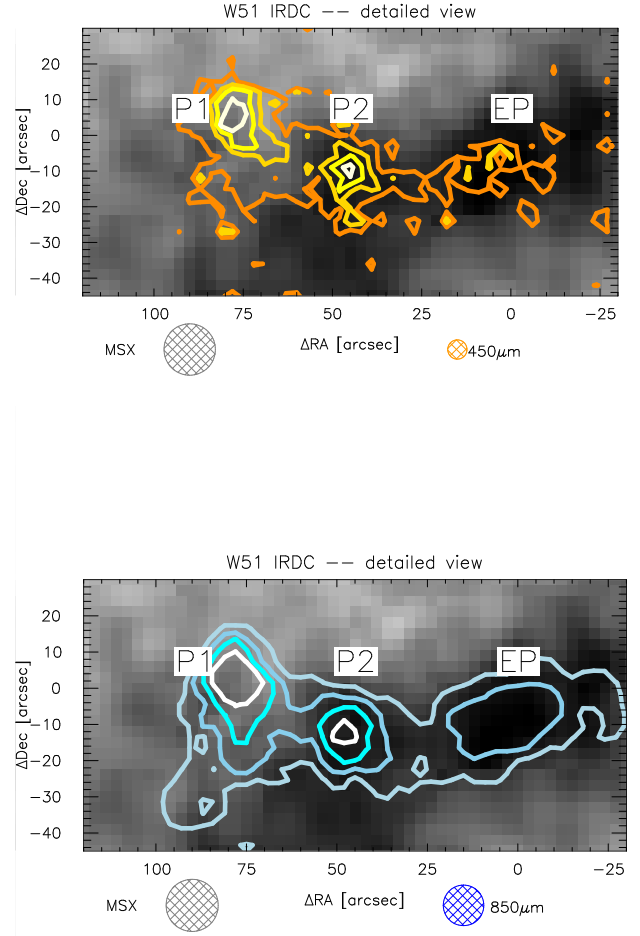


Fig. 15. MSX 8 μm continuum (greyscale) overlaid with SCUBA 450 μm contours (top panel) and SCUBA 850 μm contours (bottom panel), from Ormel et al. (2005). The zero points of the (RA,Dec) coordinate axes are ($19^{\text{h}}21^{\text{m}}44.7^{\text{s}}$, $13^{\circ}49'34.7''$). In these coordinates (ΔRA , ΔDec), our objects S5 and S6 would lie at ($74''$, $-4''$) and ($83''$, $4''$), respectively.

the mass of the central source can be anything between 0.2 and 30 M_{\odot} and the envelope accretion rate may range from 4×10^{-7} up to $10^{-2} M_{\odot}/\text{yr}$, or there may even be no envelope accretion at all.

Clearly, there is a need for more data points. In this light, the peak intensities at 450 and 850 μm from Ormel et al. (2005) can be used. It is crudely assumed that two thirds of the 450 and 850 μm flux of P1 originated from S6, the brightest of the two cores. The two data points added to the three Spitzer fluxes used to get the fits in Fig. 16 are listed in Table 7. Large uncertainties are adopted, mainly to reflect the uncertainty in the assumption of the relative contributions of S5 and S6 to the total P1 flux.

In addition, the upper limit in IRAS 100 μm – also noted by Ormel et al. (2005) – can be used as input. Nothing was detected by IRAS at this position, which means that any 100 μm emission must be below the detection limit of 90 MJy/sr. In a roughly spherical beam with a FWHM of 220'', this corresponds to ~ 80 Jy. A conservative uncertainty of 30 Jy is adopted for this upper limit.

The result of adding the sub-millimeter fluxes at 450 and 850 μm to the Spitzer data points is shown in Fig. 17. Many of the degeneracies present in the fits in Fig. 16 are now solved. The

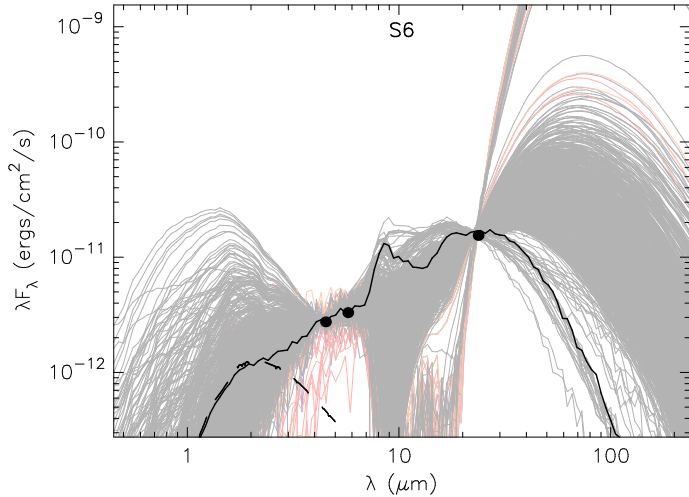


Fig. 16. The best model fits to S6, using only the 4.5, 5.8 and 24 μm data points. The black curve is the model that fits the data points with the smallest total χ^2 . The gray curves represent all other models that have a $\chi^2/N - \chi_{\text{best}}^2/N < 3$. The colored lines indicate the slight dependence on aperture for some of the fitted SEDs.

Table 7. Datapoints used for the SED fit to S6. Note that the IRAS 100 μm flux is an upper limit.

band	value	uncertainty	unit	Aperture (")
IRAC 4.5 μm	11.60	0.022	mag	15
IRAC 5.8 μm	10.65	0.117	mag	15
MIPS 24 μm	4.42	0.013	mag	25
IRAS 100 μm	< 80	30	Jy	220
SCUBA 450 μm	2.0	0.5	Jy	50
SCUBA 850 μm	0.35	0.1	Jy	80

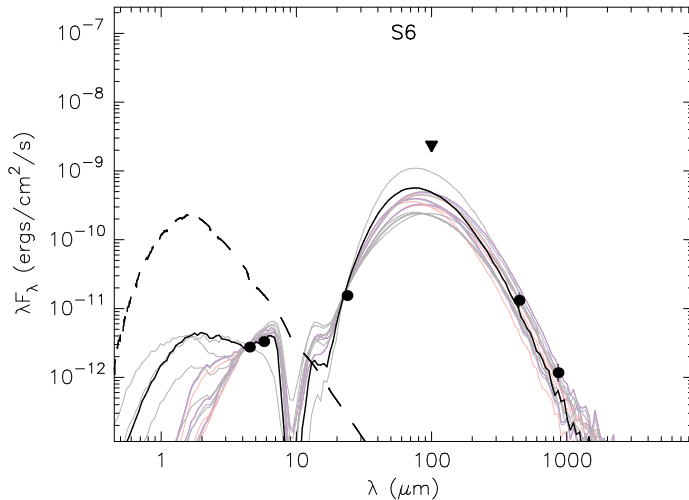


Fig. 17. The best model fits to S6, incorporating sub-millimeter fluxes, see Table 7. The solid black curve shows the best-fit YSO model. The dashed curve shows the photosphere that is used as input for the radiative transfer code. The gray curves show all YSO models that fit each datapoint with a $\chi^2/N - \chi_{\text{best}}^2/N < 3$. The colored curves show the slight dependence on aperture of some of the SEDs.

IRAS 100 μm upper limit (the triangle in the figure) is consistent with the fitted models, but does not constrain the fit further. The same set of best-fit models is obtained without the IRAS flux limit.

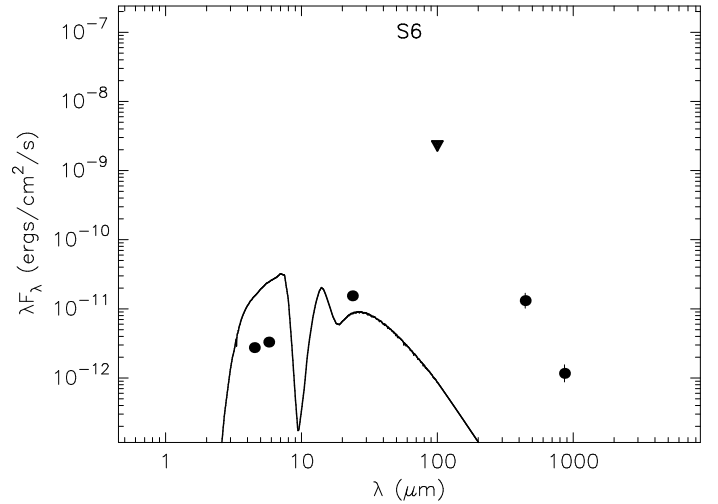


Fig. 18. The best fit stellar photosphere (solid curve) to datapoints of S6.

The stellar photosphere that fits the S6 data best is shown in Fig. 18. Judging from the fact that this is such a poor fit to the data, S6 is indeed likely to be a young stellar object.

Going back to the YSO SED fit in Fig. 17, it is possible to examine the parameters of the best-fit SED and of those SEDs that come close to the best fit. All SEDs in this figure are dominated by emission from hot dust in the circumstellar envelope: the big bump between roughly 20 and 1000 μm . Disk emission is found in the same wavelength region, but is at least an order of magnitude less than the envelope emission, especially at high wavelengths. The disk is the more dominant contributor at wavelengths < 20 μm , where emission from warmer dust is expected. The disk should be generally warmer than the envelope, since it is exposed to more of the photons from the central star.

The histograms in Fig. 19 show that the envelope accretion rate, \dot{M}_{env} , of S6 lies between 10^{-4} and $2 \times 10^{-3} M_{\odot}/\text{yr}$ and that the disk mass, M_{disk} , lies between 5×10^{-4} and $0.3 M_{\odot}$. The stellar mass, M_{\star} , ranges from 2–8 M_{\odot} ; in the best fit, $M_{\star} = 6 M_{\odot}$. The two parameters shown in the histograms in Fig. 19 are the ones that – calibrated by M_{\star} – determine the ‘Stage’ (see Table 6) in which a YSO is found to be. With fast accretion from the envelope, $\dot{M}_{\text{env}}/M_{\star} > 10^{-6} M_{\odot}/\text{yr}$ and a massive disk, $M_{\text{disk}}/M_{\star} > 10^{-6} M_{\odot}$, S6 is put in the category of Stage I objects. The age of the central protostar is found to be between 10^4 and 2×10^5 yr, its current stellar temperature (T_{\star}) between 3500 and 5500 K. The total luminosity of the object – including re-radiation from heated circumstellar dust – is put between 40 and 600 L_{\odot} ; the total luminosity of the best-fit model is 197 L_{\odot} . These values are consistent with the luminosity of P1 modeled by Ormel et al. (2005).

S5

The second brightest source at 24 μm , S5, has associated fluxes in all IRAC bands. The remaining portion of the P1 SCUBA fluxes are attributed to S5 (one third, the complement of the portion that was attributed to S6): 1 ± 0.5 Jy at 450 μm and 0.18 ± 0.1 Jy at 850 μm . Combined with the five Spitzer fluxes and the 80 Jy upper limit at 100 μm from IRAS, there are eight data points to provide as input to the SED fitting tool. The best fitting SED to these points is shown in Fig. 20. This fit is significantly worse than the SED fitted to S6. Of this fit, the total $\chi^2 \sim 5800$. Even if the datapoints at 3.6 μm and 8.0 μm are disregarded in order to match the wavelength bands used to fit the

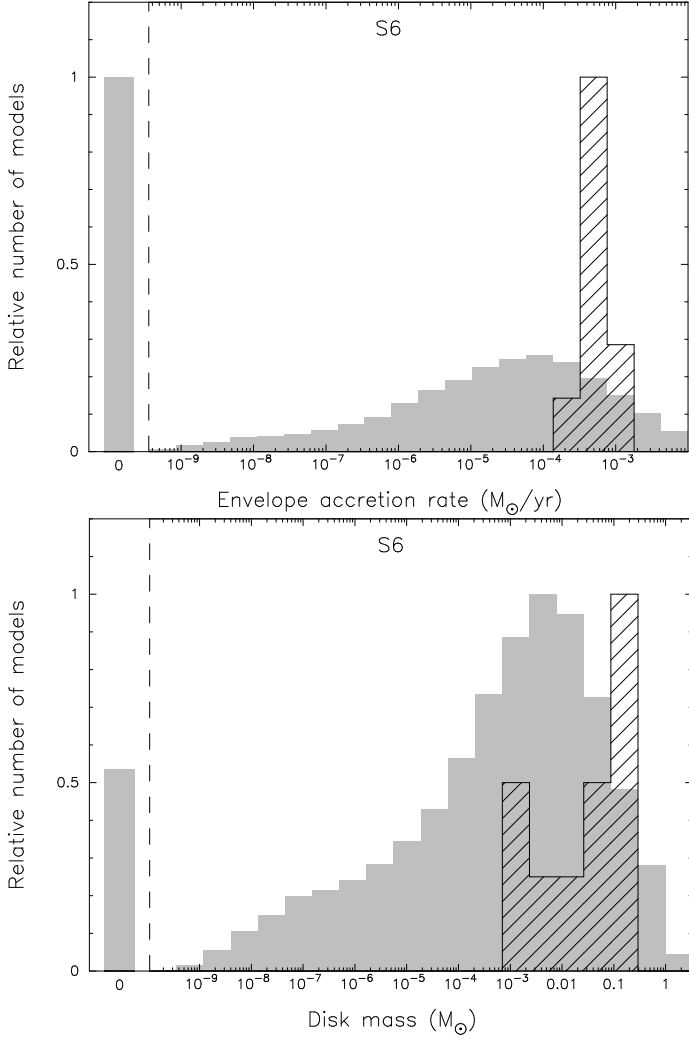


Fig. 19. Ranges of \dot{M}_{env} (top panel) and M_{disk} (bottom panel) of models that fit the data of S6. The gray histograms show the distribution of the models in the grid. The hashed histograms show the parameters of all models which have $\chi^2 - \chi^2_{\text{best}} < 3$, i.e. the model SEDs which are plotted in Fig. 17.

S6 SED, the total χ^2 of the S5 fit is ~ 800 , where $\chi^2 \sim 7$ for the S6 best-fit SED. In addition, the optimal distance of the S5 fit is 3.2 kpc, slightly large, compared to the distance estimate of the IRDC at 2.5 kpc. The best-fit stellar photosphere, however, is even worse than the best-fit YSO SED, using the same set of datapoints.

The model SED shown in Fig. 20 has $M_{\star} \simeq 6 M_{\odot}$ and $T_{\star} \simeq 4000$ K. Both the envelope accretion rate ($\dot{M}_{\text{env}} \simeq 10^{-3} M_{\odot}/\text{yr}$) and the disk mass ($M_{\text{disk}} \simeq 0.3 M_{\odot}$) are high, even compared to the stellar mass of $6 M_{\odot}$. This would classify S5 as a Stage I source, consistent with the classification of this source based on the IRAC color-color diagram in Sec. 5.1.1. The total luminosity of S5, including re-radiation from heated circumstellar dust, is $\sim 460 L_{\odot}$, as estimated by the SED fit. The parameter values listed here for S5 should be interpreted with care, bearing in mind the fact that the SED fit to the S5 datapoints is so poor.

The stellar masses of $6 M_{\odot}$ each for S6 and S5 will increase as they accrete more matter from their disks and envelopes before they reach the main sequence. With the current accretion rate, it is unlikely that they will become more massive than $\sim 10 M_{\odot}$

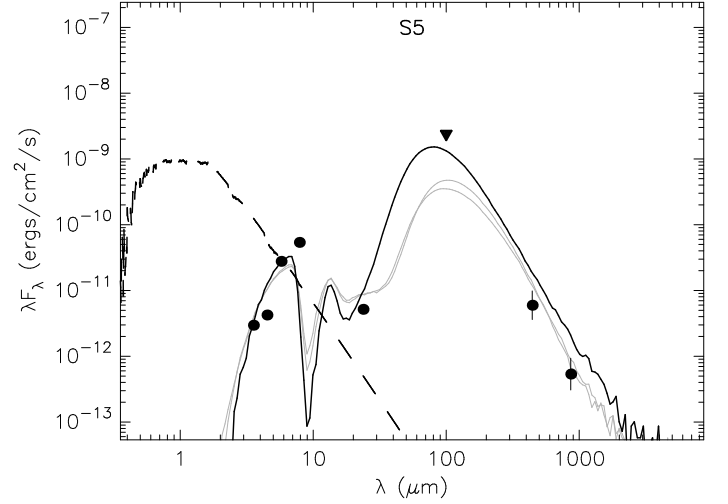


Fig. 20. The best-fit SED (solid curve) to the S5 datapoints (filled circles and one triangle for an upper limit). The dashed curve is again the stellar photosphere used as input to the radiative transfer code for this SED. The grey curves now show all other fitted SEDs with $\chi^2/N - \chi^2_{\text{best}}/N < 150$.

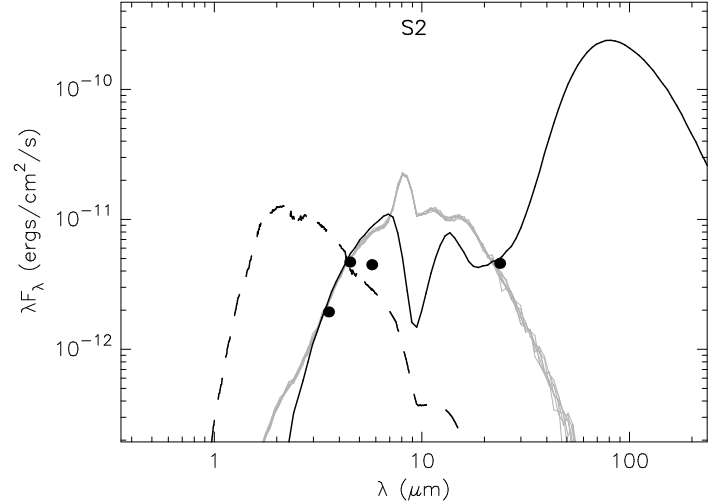


Fig. 21. The best-fit SED (solid curve) to the S2 datapoints (filled circles).

before they reach the main sequence. The total luminosity of S5 and S6 together is $\sim 600 L_{\odot}$, which is still consistent with the values modeled by Ormel et al. (2005).

5.2.3. Fitting other cores

Besides the two brightest cores, there are nine other cores which have a MIPS detection and a total of at least three fluxes, the minimum number of datapoints required for the SED fitter. These cores are S2, S4, S8, S13, S14, S15, S17, S18 and S19. Of these, S2, S15, S14, S13 and S8 appear to be spatially associated to the IRDC filament (see Fig. 14 and Table 8) and will be discussed first.

S2

In Fig. 21, the YSO SEDs that fit best to the S2 datapoints are shown. The solid black curve shows the best-fit SED, with a total χ^2 of 37. Some of the gray curves – radically different SEDs – have slightly higher χ^2 values, but still below 40. If the best-fit SED in this case is indeed the best description for the object, it

Table 8. All twenty MIPS sources and the Stage in which they are found to be. Column (1) lists the name of the object, corresponding to the entry in Table 4. Column (2) indicates whether the source is thought to be spatially associated to the IRDC filament. The number of available datapoints, N , is listed in column (3). If N is at least three, the source is fitted to the model grid of SEDs. If so, χ^2/N (see Eq. 7) is given in column (4). Column (5), (6) and (7) list the fitted stellar mass, envelope accretion rate and disk mass, respectively. Note that the latter two are given in terms of M_\star , not M_\odot . In column (8), the Stage is indicated in which the source falls according to the values in columns (6) and (7) (see Table 6 for the Stage definitions). If the source is fitted, but not classified as a YSO, this is also indicated in column (8). If a source does not have $N \geq 3$, its evolutionary stage is assessed by considering (limits to) the $[8.0] - [24]$ color index (see Sec. 5.2.4); in these cases, the Stage is indicated between square brackets.

source (1)	associated (2)	N (3)	χ^2/N (4)	M_\star (5)	$\dot{M}_{\text{env}}/M_\star$ (6)	M_{disk}/M_\star (7)	Stage (8)
S1	yes	1	-	-	-	-	[I]
S2	yes	4	9.6	$4 M_\odot$	0	9×10^{-8}	III
S3	no	1	-	-	-	-	[I]
S4	no	4	54	-	-	-	photosphere
S5	yes	7	836	$6 M_\odot$	2×10^{-4}	5.4×10^{-2}	I
S6	yes	5	1.35	$6 M_\odot$	6×10^{-5}	1.3×10^{-2}	I
S7	yes	2	-	-	-	-	[I]
S8	yes	5	26	$3.7 M_\odot$	0	2×10^{-7}	III
S9	yes	2	-	-	-	-	[I or II]
S10	no	1	-	-	-	-	[I]
S11	yes	1	-	-	-	-	[I]
S12	yes	1	-	-	-	-	[I or II]
S13	yes	4	88	$14 M_\odot$	5×10^{-4}	0	I
S14	yes	5	22.5	$5 M_\odot$	0	1.3×10^{-8}	III
S15	yes	3	0.25	$2.5 M_\odot$	0	1.5×10^{-3}	II
S16	yes	1	-	-	-	-	[I or II]
S17	no	5	839	-	-	-	photosphere
S18	no	5	405	-	-	-	photosphere
S19	no	3	7.7	-	-	-	photosphere
S20	no	1	-	-	-	-	[I or II]

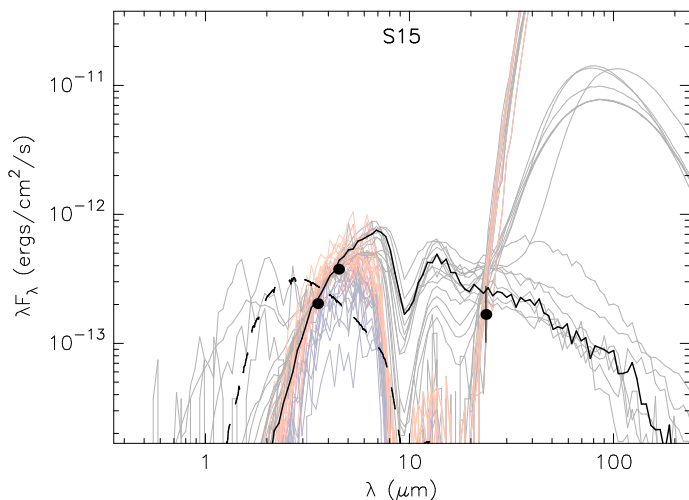


Fig. 22. All SEDs to the S15 datapoints (filled circles) that fit with $\chi^2/N - \chi_{\text{best}}^2/N < 1$.

is clearly a Stage I source ($\dot{M}_{\text{env}} \approx 3 \times 10^{-4}$ and $M_\star = 1.5 M_\odot$). However, if one of the grey models is the correct description, $\dot{M}_{\text{env}} = 0$, which is why the bump in the SED longward of $20 \mu\text{m}$ disappears. Considering the fact that little or no emission is observed at this position at sub-mm wavelengths by SCUBA (Ormel et al. 2005), the latter of the two options (no envelope accretion) is deemed the most probable. In this case, $M_\star \approx 4 M_\odot$. These model SEDs are dominated by disk flux, although the disk mass is fairly modest at $M_{\text{disk}}/M_\star \approx 9 \times 10^{-8}$, which classifies S2 as a Stage III object.

S15

Fig. 22 shows an example of a badly constrained model fit. Using only the three flux values at 3.6 , 4.5 and $24 \mu\text{m}$ available for S15, most parameter values are not constrained better than to four or more orders of magnitude, even considering only those fits with $\chi^2/N - \chi_{\text{best}}^2/N < 1$. Introducing an upper limit of 3 mJy in the $8 \mu\text{m}$ band (where no flux is found for this source) does not help to constrain the range of possible SED fits. S15 is the faintest of the twenty sources in MIPS $24 \mu\text{m}$ (magnitude 9.3) and has a large uncertainty in its magnitude. The large uncertainty in the flux influences the SED fitting routine in two respects. First, there are many possible SEDs at the $24 \mu\text{m}$ point, because the flux at this point is not well constrained (see the error bar in the datapoint in Fig. 22). Second, the χ^2 value drops significantly due to the large σ value (cf. Eq. 7), while this does not in fact indicate a good fit.

S14

S14 is seen in all four bands of IRAC, in addition to the MIPS band. The five datapoints provided to the model SED fitter give a tightly constrained set of fitting SEDs, shown in Fig. 23. The total of five SEDs that fit this data at all are all shown. The best fit has a total χ^2 of 113; the χ^2 values for the other four fits range up to only 141. In fact, the five fits are all the same model YSO, the only difference is the viewing angle. According to the fitted models, S14 is in a fairly advanced phase of evolution: there is no envelope accretion and very little disk accretion ($\dot{M}_{\text{disk}} \approx 6 \times 10^{-12} M_\odot/\text{yr}$). This is reflected in the SED by the fact that the stellar photosphere (the dashed curve in Fig. 23) is hardly extinguished at wavelengths $\lesssim 2 \mu\text{m}$. The mid-IR flux explained by the disk ($M_{\text{disk}} \approx 6.5 \times 10^{-8} M_\odot$). The central star has parameters readily consistent with the main sequence mass-luminosity relation (Böhm-Vitense 1992): $M_\star = 5 M_\odot$,

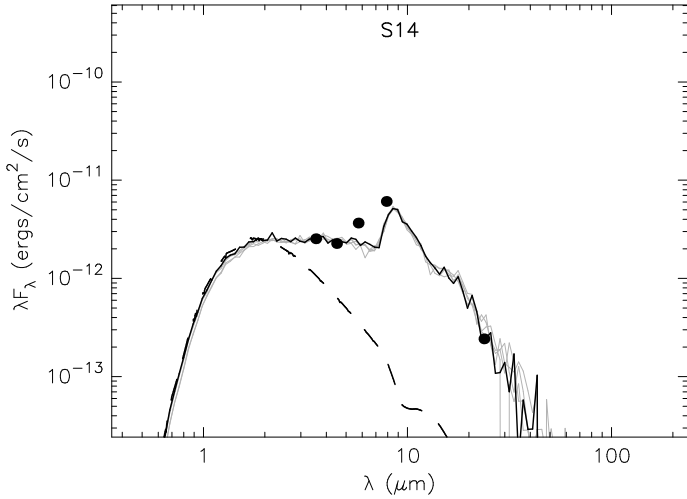


Fig. 23. All SEDs that fit to the five S14 datapoints. The dashed curve shows the input stellar photosphere, which in this case provides a significant contribution to the total energy output of the object.

$T_{\star} = 16600$ K and the total luminosity – which can be assumed to be either direct flux from the star or stellar energy re-radiated by the heated disk – is $L_{\text{tot}} \approx 500 L_{\odot}$. S14 is an O-type star near the end of its protostellar phase, in Stage III.

S13

S13 has well-determined fluxes in MIPS in and the first three IRAC bands, but none in the IRAC $8.0 \mu\text{m}$ band. Unlike the case of S15 described above (page 22), it does have an impact for S13 when an upper limit on the IRAC $8.0 \mu\text{m}$ flux is fed to the SED fitter. What would otherwise have been fitted as an object without any envelope accretion, is now fitted with an SED of a very massive central star ($\sim 14 M_{\odot}$) with rapid envelope accretion, $\dot{M}_{\text{env}} = 7 \times 10^{-3} M_{\odot}/\text{yr}$: clearly a Stage I object. It would certainly help in this case to add sub-millimeter fluxes in order to constrain the envelope-dominated part of the SED at the very long wavelengths.

S8

S8 has colors in all IRAC bands and the first MIPS band, so it was placed in the IRAC+MIPS color-color diagram (Fig. 13), where it was found to be on the edge of the ‘mostly Stage II’ and ‘mostly stage III’ regions. The SED model fits to the same five datapoints are shown in the top panel of Fig. 24. It is evident that the set of model fits shown here is very degenerate with respect to the physical properties of the object we are trying to extract. Especially in the near-IR regime, the range of SEDs diverges. This can be constrained by making use of the 2MASS catalog, which contains point source fluxes in the J ($1.25 \mu\text{m}$), H ($1.65 \mu\text{m}$) and K_s bands in a large portion of the sky, including our field. No 2MASS entries are found near the position of S8, however. The 2MASS limiting magnitudes can then be used as upper limits: magnitude 15.8, 15.1 and 14.3 for J, H and K_s bands, respectively (Skrutskie et al. 2006). S8 is now found to have a stellar mass of $3.7 M_{\odot}$ and no envelope accretion. In addition, the disk mass is very low, $M_{\text{disk}}/M_{\star} = 2 \times 10^{-7}$, which classifies this source as a Class III object.

S4, S19

The MIPS sources that do not seem to be spatially associated to the IRDC are S4, S17, S18 and S19. The datapoints of both S4 and S19 are fit by a stellar photosphere (without any circumstel-

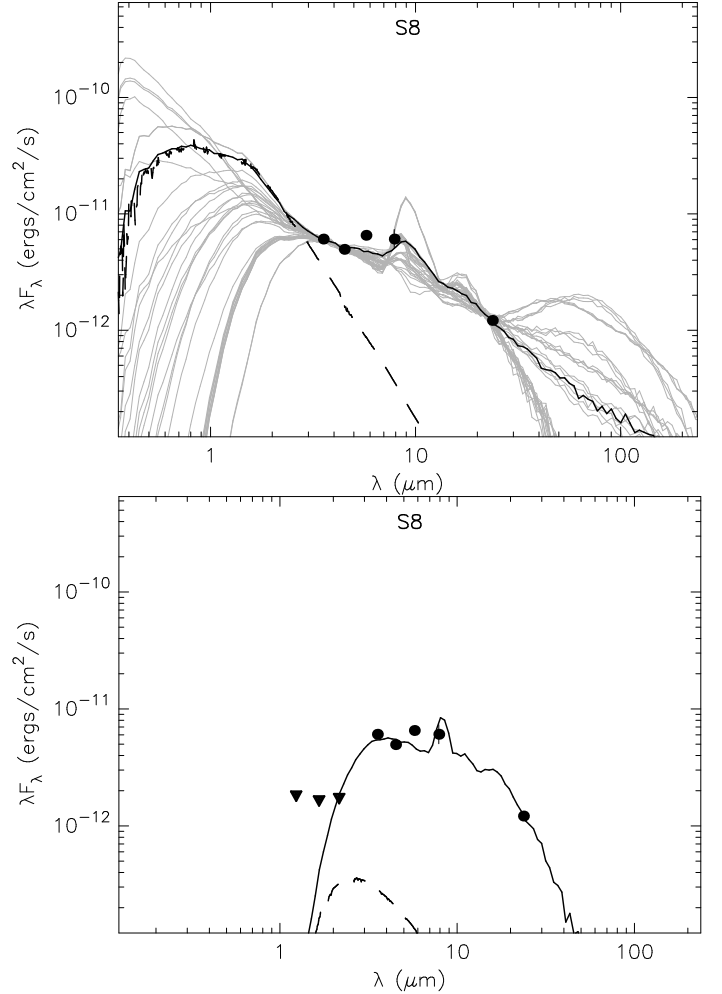


Fig. 24. Model SED fits to the Spitzer datapoints of S8 (top panel) and with the 2MASS upper limits imposed (bottom panel). Note that the scale along the wavelength axis is not equivalent in both panels.

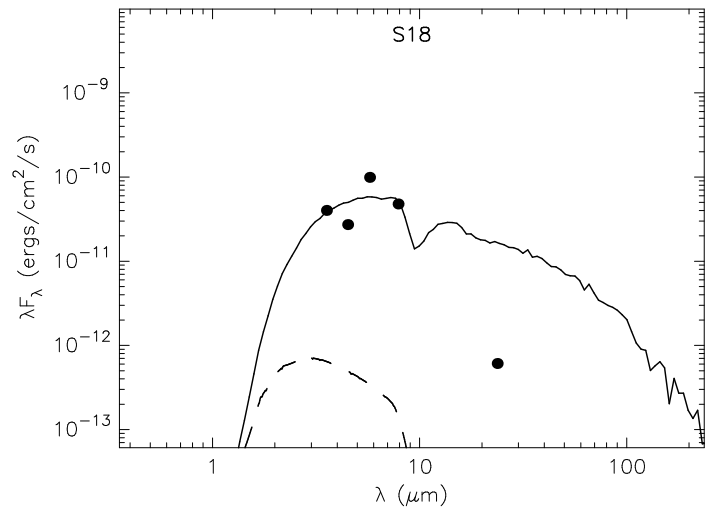


Fig. 25. The poor YSO SED model fit to the datapoints of S18.

lar photosphere) with a significantly lower χ^2 than when fitted to a YSO SED. It is most sensible at this point to discard the possibility that these objects are in fact YSOs. With a stellar photospheric temperature of 3400 K, S4 is an early-type M-star and S19, with $T_{\text{eff}} = 4700$ K, is an early-type K-star.

S17, S18

An analogous argument holds for S17 and S18: their datapoints are fit by a stellar photosphere SED with a lower χ^2 than by a YSO SED. The difference with respect to S4 and S19 is that, although the YSO SED fit is poor for S17 and S18 (for reference, the best-fit YSO SED to S18 datapoints is shown in Fig. 25), the stellar photosphere fit is poor on itself. Both sources are found to be strangely blue in the [8.0] – [24] color in Sec. 5.1.5. The model fitter again shows difficulty reconciling the relatively high IRAC fluxes with the low – but non-zero – 24 μm flux.

There are entries in the 2MASS archive at the positions of both S4 and S18. The addition of these datapoints does not provide better fits, nor does it constrain the possible range of model fits. The nature of S18 becomes more unclear when the near-IR fluxes are taken into account, both the YSO fit and the photosphere fit deteriorate. For S4, the fitted photosphere of $T_{\text{eff}} = 4500$ K, peaking in the 2MASS K_s band (2.17 μm), is confirmed by the 2MASS datapoints.

5.2.4. Lack of datapoints for nine MIPS cores

Some interesting MIPS cores can not be placed in a color-color diagram or be fitted to a model SED, due to a lack of datapoints (all sources with $N < 3$ in Table 8). However, the fact that each of these sources shows 24 μm emission does make them YSO candidates. Of these, S3, S10 and S20 are not associated to the cloud, the other six are.

Stage I candidates: S1, S3, S7, S10, S11

Based on a limiting magnitude of 11.3 in IRAC 8.0 μm (see Table 3), the [8.0] – [24] colors of S1, S3, S7, S10 and S11 are all ≥ 4 . This places all these sources in a convincing position in IRAC+MIPS color-color space (Fig. 9) to be classified as a Stage I objects.

Stage I/II candidates: S9, S12, S16, S20

The same IRAC [8.0] limit can be imposed on three other sources. The [8.0] – [24] colors of S12, S16 and S20 are ≥ 2.9 , ≥ 3.3 and ≥ 3.9 , respectively. This places such constraints on the position of these sources in the IRAC+MIPS color-color diagram (rightmost panel in Fig. 9) that they are likely to be either Stage II or Stage I objects. The [8.0]–[24] color of S9 is 3.5, possibly placing it on the edge of the Stage I region in IRAC+MIPS color-color space.

5.2.5. Summary of SED fitting results

As is seen in the overview in Table 8, the sources that are successfully fitted to a YSO SED are all spatially associated to the cloud. Sources which are fit better by photosphere models or not at all, lie away from the dark cloud. The YSO objects identified as such range from Stage I to III and have core masses ranging from 2.5–14 M_{\odot} .

The total luminosity of the YSO model fits to S5 and S6 combined is consistent with the central heating source of P1, modeled by Ormel et al. (2005), within their 1σ limits.

6. Discussion

6.1. Contamination of YSO sample

For the analysis in Chapters 5.1 and 5.2, the assumption is made that all sources in the G48 field showing mid-IR excess are young stellar objects (YSO). However, there are other physical processes known that can cause mid-IR excess, most notably those in AGB stars, extincted photospheres and (star forming) galaxies. In this section, we show that it is unlikely that the YSO content of G48 is contaminated by these categories of objects.

6.1.1. AGB stars

An Asymptotic Giant Branch (AGB) object is a star of $M \lesssim 8M_{\odot}$ at the end of its lifetime. In the AGB phase, after depleting the hydrogen in its core, it ejects its outer layers, while at the same time cooling down these outer layers of the star. This mass loss process results in a relatively cool envelope of dust, which is heated by the central star. Some of the physical processes that occur in YSO, occur also in AGB envelopes. As Marengo et al. (2006) and Groenewegen (2006) point out, based on observationally calibrated numerical codes, IRAC and MIPS color indices of AGB objects show significant infrared excess. The [3.6] – [4.5] colors can range from –0.3 to 1.3 and [5.8] – [8.0] colors may range from –0.2 to at least 1.3. (cf. the color-color diagrams in Chapter 5.1). Groenewegen (2006) also shows that [8.0] – [24] model colors of AGB and post-AGB objects can range from 0 to 3.5. This range again coincides with part of the color spread of YSO models in Fig. 8.

There is no evidence to support that the overall density of AGB stars is enhanced in the particular direction of the IRDC under investigation. This means we can use a Galactic density model of AGB stars to estimate how many of these objects can be expected to be observed in the $5 \times 5'$ *Spitzer* field.

According to Wainscoat et al. (1992), who provide such a model, the most important components in which to find stellar objects in the infrared are the Galaxy's disk, the arms and the ring. The halo is generally unimportant, even more so at low galactic latitude. The Galactic bulge is not an important contributor at large distances from the Galactic center.¹⁵ Summing up all classes of AGB stars listed in the article, the disk model predicts an AGB density of $\sim 160 \text{ kpc}^{-3}$ in the solar neighborhood. The density decreases exponentially with distance from the Galactic center and it decreases – with a different exponential scale height – with increasing 'vertical' distance from the Galactic plane. Assuming a galactic latitude of 0 (G48 is at $b = -0.3$ in reality) results in an overestimate of the AGB density.

In Eq. 4 from Wainscoat et al. (1992), $z = 0$ (galactic latitude 0) is substituted and $\rho_D(S)$ is replaced by the total disk density of all varieties of AGB in the solar neighborhood: $\sim 160 \text{ kpc}^{-3}$. The galactocentric distance R can be written in terms of the line of sight distance r : $R(r) = \sqrt{r^2 + R_0^2 - 2 \cos(\ell)R_0r}$, for lines of sight in the Galactic plane at galactic longitude ℓ . This yields a simplified expression for the density of AGB (per kpc^3) in the disk as a function of line of sight distance r in kpc:

$$\rho_{\text{disk}}(r) \approx 160 \exp\left(-\frac{\sqrt{r^2 + R_0^2 - 2 \cos(\ell)R_0r} - R_0}{h}\right). \quad (8)$$

¹⁵ Our line of sight passes the Galactic center at a minimum distance of 6.4 kpc.

The same values as in Wainscoat et al. (1992) are assumed for R_0 , the distance from the Sun to the Galactic center (8.5 kpc), and the disk scale height h (3.5 kpc).

All objects observed in the field of view must be spatially located in a pyramid of volume $V = \frac{1}{3} (\tan(\alpha))^2 d^3$, where α is the angular size of a side of the square field of view (in this case $5'$) and d is the maximum distance at which sources are visible. An infinitesimal slice of this pyramid at distance r from the observer has volume $r^2 \tan^2(\alpha) dr$. Now, substituting the values for R_0 and h into Eq. 8, multiplying by the volume and integrating from 0 to the maximum distance d , an expression for the total number of AGB stars expected in our field is obtained in Eq. 9. In this equation, an additional factor of 5 is included to take into account the assumption that the arms and the ring together do not contribute more than four times the amount of AGB as the disk does.

$$N_{\text{AGB}}(d) \approx 5 \int_0^d \rho_{\text{disk}}(r) \tan^2(5') r^2 dr \\ \approx 0.0017 \int_0^d r^2 \exp\left(-\frac{\sqrt{r^2 - 11.24r + 72.25} - 8.5}{3.5}\right) dr, \quad (9)$$

with d in kpc.

Assuming that IRAC detects all AGB up to a distance of 20 kpc (well into the outskirts of the opposite side of the Galaxy), a numerical integration of Eq.9 yields a total of only 2.5 AGB in our field.

The simplifying assumptions made above are chosen such that none induce an underestimate of N_{AGB} . In fact, most of them accumulate to (greatly) overestimate the total amount of expected AGB stars; a more accurate calculation would yield an even smaller number, possibly by orders of magnitude. The estimate in Eq. 9 can therefore be regarded as an extreme upper limit and it is safe to state that it is very unlikely that any of the sources in our field is an AGB star.

6.1.2. Extincted photospheres

Stellar photospheres, in the absence of extinction, are expected to show no infrared excess, i.e. they lie near the (0,0) locus in the IRAC and IRAC+MIPS color-color diagrams. One can find the region in color-color space where reddened photospheres might be found, from the reddening vectors in Fig. 9, representing an A_V extinction of 20. In the IRAC color-color distribution of our objects (Fig. 10), only two objects fall in the region that may be occupied by reddened stellar photospheres. These two would have to be extincted as strongly as $A_V > 40$, assuming the Indebetouw et al. (2005) extinction law.

In the photosphere model fit to S4, the best-fit A_V extinction is 20. As is noted in Sec. 5.2.3, this photosphere model is indeed the best fit to the datapoints for S4, ranging from near-IR (2MASS) up to MIPS 24 μm . Still, for photospheres to be visible at 24 μm , they would have to be highly extincted as well as intrinsically very cold, e.g. S4 is fitted to have a stellar temperature of 4500 K.

6.1.3. Background galaxies

Other galaxies consist of a wide variety of objects, including possible star-forming regions, AGB objects and active galactic nuclei. All of these are known to give rise to emission in the infrared regime. The combined light from an (unresolved) galaxy – an ensemble of stars, gas, dust and possibly black holes –

might show mid-IR characteristics similar to those of an individual YSO associated to the IRDC.

A search through the NASA/IPAC extragalactic database results in two galaxies within our field of view. Neither of these coincide with any $24\ \mu\text{m}$ or $8\ \mu\text{m}$ detections in the list in Table 4, nor to any visible emission cores in the mosaics of the other three bands.

It is concluded that the only two known extragalactic objects in our field are not seen by IRAC or MIPS $24\ \mu\text{m}$. This is probably due to the high extinction through the mid-plane of the Galaxy. Therefore, there is no need for concern about possible contamination of our YSO sample by background galaxies.

6.2. Mid-IR counterparts of P2 and EP

The modeling of P2 and EP (see Fig. 15) in Ormel et al. (2005) indicates luminosity sources of $30\text{--}1000\ L_{\odot}$ for P2 and $2\text{--}100\ L_{\odot}$ for EP. This modeling, using only the SCUBA sub-millimeter data and the upper limit in IRAS $100\ \mu\text{m}$, implies similar conditions in the inner cores of P2 and P1. Yet, P1 is detected by Spitzer as two bright sources at 8 and $24\ \mu\text{m}$, while EP and even P2 show no emission at all at these mid-IR wavelengths.

It is noted that P2 and EP lie deeper into the extinction, while P1 lies more to the edge of the dark cloud filament. The optical depth at the positions of P2 and EP is determined to be >1 at $8\ \mu\text{m}$ (MSX) by Ormel et al. (2005). Using comparative dust opacities from Ossenkopf & Henning (1994), $24\ \mu\text{m}$ emission is expected to be still optically thick. Extinction due to the cloud in which both sources are embedded could therefore be an explanation for the lack of emission in the Spitzer mid-IR bands.

6.3. Future work

In the near future, we plan to publish a paper on the data presented in this thesis and the conclusions that can be drawn based on these data. A summary of issues that need to be addressed in the paper, but were not in this thesis, is given here.

- Definition of some sort of a ‘perpendicular’ tangential distance to the IRDC filament for every source. This will help identifying YSO candidates which are *associated* to the IRDC.
- A full systematic merging of the Spitzer source list in Table 4 to the 2MASS catalog. This will provide the opportunity to fit sources that have only one or two Spitzer fluxes if they have 2MASS counterparts. For sources that already have sufficient (≥ 3) datapoints in the Spitzer passbands, possible 2MASS counterparts (or upper limits if no counterpart is found) could help constrain the model parameters.
- Fitting of sources that do have at least 3 datapoints, but are not detected in MIPS $24\ \mu\text{m}$. Although the primary focus was placed on $24\ \mu\text{m}$ cores (see Sec. 5.2), the sources that do *not* show $24\ \mu\text{m}$ emission are in fact more likely to be later type YSOs, since it is primarily the accreting envelope that provides emission at wavelengths $\gtrsim 20\ \mu\text{m}$.

7. Conclusions

The main scientific conclusions from this thesis work are listed here.

- The spread of sources in the G48 field in IRAC color-color space (Fig. 10) is consistent with YSO models ranging from early phase Stage I sources to Stage III sources.
- Out of a total of 54 sources placed in the IRAC color-color diagram (Fig. 10), 14 sources are Stage I candidates (upper panel of Fig. 11). In addition, 28 other sources (indicated in the bottom panel of Fig. 11) are marked as general YSO candidates (Stage I, II or III). Five sources are marked as possible photospheres.
- If sources are found in regions in color-color space (see Sec. 5.1) that are irreconcilable with any YSO colors, they may be described by a stellar photosphere (e.g. S17 and S18 in Sec. 5.2.3).
- The objects S8 and S14 are both classified as either Stage II or Stage III objects, based on their position in the color-color diagrams (Fig. 13 and 10); this is confirmed by detailed SED model fitting, classifying both sources as early Stage III objects.
- The sources S5, S17 and S18 are marked as Stage I candidates from color-color diagram analysis. For S5, this is confirmed by SED fitting. S17 and S18 however, appear more likely to be stellar photospheres from SED modeling results.
- Model SED fits to individual sources show that YSOs lie preferentially along the IRDC extinction filament.
- Seven cores are identified as YSOs by model SED fitting: three Stage I objects, one Stage II object and three Stage III objects. The best-fit stellar masses range from 2.5 to $14\ M_{\odot}$.
- The emission peak P1, identified by Ormel et al. (2005), is resolved by Spitzer into two distinct cores: S5 and S6. Both objects fit to YSO models with envelope accretion rates exceeding $10^{-2}\ M_{\odot}/\text{yr}$. Each source has a fitted stellar mass of $\sim 6\ M_{\odot}$. From the SED fits, the total luminosity of S5 and S6 combined is $\sim 660\ L_{\odot}$, consistent with the modeling results found by Ormel et al. (2005) for P1.
- The lack of mid-IR counterparts to the sub-millimeter detections at P2 and EP (Ormel et al. 2005) may be caused purely by geometrical effects. Regardless of the circumstellar material that is dynamically associated to the cores, these cores may be embedded deeply in the surrounding cloud or lie behind it in our line of sight.
- The SED fitting utility is a powerful tool for determining physical properties of a YSO. In addition to $2\text{--}10\ \mu\text{m}$ data (from e.g. IRAC), data at longer wavelength (e.g. MIPS $24\ \mu\text{m}$) is often crucial in constraining the set of possible YSO model fits. It is best to have datapoints or upper limits in many different regimes of the wavelength spectrum, i.e. not only in the mid-IR, but also in the near-IR, far-IR, and sub-millimeter.
- The data and the analysis introduce a bias towards (i) the more massive YSOs, which are intrinsically bright and (ii) early-stage YSOs, which are relatively bright at wavelengths $> 20\ \mu\text{m}$. In addition to the YSOs classified in this thesis, less massive and later-stage YSOs are expected to be found from further study of the data.

Acknowledgements

There are some people who I would like to thank for making this whole project possible, enjoyable and successful.

- First of all: Russell, my advisor, for showing excitement about scientific results and caring about sound data reduction and good statistics at the same time. He reminded and taught me how important it is to make *use* of available knowledge, but let me climb up the learning curve when I wanted to. Our ‘quick’ deliberations often resulted in unexpectedly long conversations on science, data reduction, statistics, teaching, life, the Universe and Everything.
- Thomas Robitaille, for answering many questions on the set of YSO models and the fitting tool; for making adjustments and improvements to the fitting tool on request; and all this generally very swiftly, often late at night, in the middle of the weekend, or both.
- The people at the Spitzer Science Center helpdesk, for answering questions on MOPEX and its documentation.
- Wilfred, who participated in many brainstorm sessions about where to go with the data and the science, and provided the beautiful three-color composite image of our IRDC.
- Marco, for acting as interim-supervisor during the summer and trying to show me the meaning of the word ‘planning’ for the first time in my life.
- Chris, for debating the interpretation of the results, and for reading parts of my thesis on very short notice and providing helpful comments.
- My roommates in ZG192 and later those in ZG193 – and other concerned (graduate) students –, who all helped in one way or another; sometimes in programming or scientific issues, sometimes in the quintessential recreational activities (inside or outside the institute) and at other times making up competitions for making it to the institute early in the morning.
- Beatrijs, who, especially in the last stage of my thesis work, has seen less of me than the average person listed above, but supported me unconditionally and helped me digest hurdles and results in the project (and sometimes explicitly told me *not* to think about the project for a moment). I will make it up to you.

Appendix A: List of acronyms

2MASS	Two Micron All Sky Survey
AGB	Asymptotic Giant Branch (star)
CCD	Coupled Charge Device
far-IR	Far-infrared (roughly 30–200 μm)
FWHM	Full Width at Half Maximum
G48	The Infrared Dark Cloud under consideration in this thesis
GLIMPSE	Galactic Legacy Infrared Mid-Plane Survey Extraordinaire
IR	Infrared
IRAC	InfraRed Array Camera
IRAS	InfraRed Astronomical Satellite
IRDC	InfraRed Dark Cloud
JCMT	James Clerk Maxwell Telescope on Hawaii
mid-IR	Mid-infrared (roughly 2–30 μm)
MIPS	Multiband Imaging Photometer for Spitzer
MIPSGAL	MIPS inner GALactic plane survey
MOPEX	Software package for MOsaicing and Point source EXtraction
MSX	Midcourse Space eXperiment
near-IR	Near-infrared (roughly 0.8–2 μm)
PAH	Polycyclic Aromatic Hydrocarbon
PRF	Point Response Function
S/N	Signal to noise ratio
SCUBA	Submillimeter Common User Bolometer Array
SED	Spectral Energy Distribution
SSC	Spitzer Science Center
YSO	Young Stellar Object(s)
ZG192	Room 192 in the ‘Zernikegebouw’
ZG193	Room 193 in the ‘Zernikegebouw’

References

- Adams, F. C., Lada, C. J., & Shu, F. H. 1987, *ApJ*, 312, 788
- Benjamin, R. A., Churchwell, E., Babler, B. L., et al. 2003, *PASP*, 115, 953
- Böhm-Vitense, E. 1992, 16
- Bok, B. J. & Reilly, E. F. 1947, *ApJ*, 105, 255
- Carey, S. J., Egan, M. P., Kuchar, T. A., et al. 2000, in *Bulletin of the American Astronomical Society*, 516–+
- Egan, M. P., Shipman, R. F., Price, S. D., et al. 1998, *ApJ*, 494, L199+
- Evans, II, N. J. 1999, *ARA&A*, 37, 311
- Fazio, G. G., Hora, J. L., Allen, L. E., et al. 2004, *ApJS*, 154, 10
- Frieswijk, W. F. W., Teyssier, D., Shipman, R. F., & Hily-Blant, P. 2005, *Protostars and Planets*
- Groenewegen, M. A. T. 2006, *A&A*, 448, 181
- Indebetouw, R., Mathis, J. S., Babler, B. L., et al. 2005, *ApJ*, 619, 931
- Klessen, R. S. 2001, *ApJ*, 550, L77
- Lada, C. J. & Lada, E. A. 2003, *ARA&A*, 41, 57
- Makovoz, D. & Khan, I. 2005, in *ASP Conf. Ser. 347: Astronomical Data Analysis Software and Systems XIV*, ed. P. Shopbell, M. Britton, & R. Ebert, 81–+
- Makovoz, D. & Marleau, F. R. 2005, *PASP*, 117, 1113
- Marengo, M., Hora, J. L., Barmby, P., et al. 2006, *ArXiv Astrophysics e-prints*
- Ormel, C. W., Shipman, R. F., Ossenkopf, V., & Helmich, F. P. 2005, *A&A*, 439, 613
- Ossenkopf, V. & Henning, T. 1994, *A&A*, 291, 943
- Perault, M., Omont, A., Simon, G., et al. 1996, *A&A*, 315, L165
- Rathborne, J. M., Jackson, J. M., Chambers, E. T., et al. 2005, *ApJ*, 630, L181
- Rathborne, J. M., Jackson, J. M., & Simon, R. 2006, *ApJ*, 641, 389
- Reach, W. T., Megeath, S. T., Cohen, M., et al. 2005, *PASP*, 117, 978
- Rieke, G. H., Young, E. T., Engelbracht, C. W., et al. 2004, *ApJS*, 154, 25
- Robitaille, T. P., Whitney, B. A., Indebetouw, R., & Wood, K. 2007, *ApJS*, accepted (astro-ph/0612690)
- Robitaille, T. P., Whitney, B. A., Indebetouw, R., Wood, K., & Denzmore, P. 2006, *ApJS*, 167, 256
- Shipman, R. F., Frieswijk, W., & Helmich, F. P. 2003, in *ASP Conf. Ser. 287: Galactic Star Formation Across the Stellar Mass Spectrum*, ed. J. M. De Buizer & N. S. van der Blik, 252–256
- Shu, F. H., Adams, F. C., & Lizano, S. 1987, *ARA&A*, 25, 23
- Simon, R., Jackson, J. M., Rathborne, J. M., & Chambers, E. T. 2006a, *ApJ*, 639, 227
- Simon, R., Rathborne, J. M., Shah, R. Y., Jackson, J. M., & Chambers, E. T. 2006b, *ApJ*, 653, 1325
- Skrutskie, M. F., Cutri, R. M., Stiening, R., et al. 2006, *AJ*, 131, 1163
- Wainscoat, R. J., Cohen, M., Volk, K., Walker, H. J., & Schwartz, D. E. 1992, *ApJS*, 83, 111
- White, R. J., Greene, T. P., Doppmann, G. W., Covey, K. R., & Hillenbrand, L. A. 2007, in *Protostars and Planets V*, ed. B. Reipurth, D. Jewitt, & K. Keil, 117–132
- Whitney, B. A., Wood, K., Bjorkman, J. E., & Cohen, M. 2003, *ApJ*, 598, 1079
- Young, C. H., Jørgensen, J. K., Shirley, Y. L., et al. 2004, *ApJS*, 154, 396

Table 4. The complete list of merged point sources. Right ascension (RA) and declination (Dec.) are listed in decimal degrees, relative of RA = 290° (19^h20^m) and Dec = +13°, J2000. The magnitudes in the four IRAC bands and one MIPS band, [3.6], [4.5], [5.8], [8.0] and [24], are calculated in section 2.3. The corresponding uncertainties ($\sigma_{[b]}$) are calculated in section 2.4. The last column (ap.phot.) contains a flag indicating whether the brightness of the object was determined by aperture photometry: (i) only in band 4 of IRAC, [8.0], in which case the flag is set to ‘4’; (ii) only in the MIPS 24 μ m band, [24], the flag is set to ‘5’; (iii) in both [8.0] and [24.0], the flag is set to ‘45’; (iv) none of the bands, the flag is ‘0’.

name	RA –290 (degrees)	Dec. –13 (degrees)	[3.6] (mag)	$\sigma_{[3.6]}$ (mag)	[4.5] (mag)	$\sigma_{[4.5]}$ (mag)	[5.8] (mag)	$\sigma_{[5.8]}$ (mag)	[8.0] (mag)	$\sigma_{[8.0]}$ (mag)	[24] (mag)	$\sigma_{[24]}$ (mag)	ap. phot. flag
S001	0.45887	0.79901	-	-	-	-	-	-	-	-	7.34	0.054	0
S002	0.45923	0.80528	12.72	0.022	11.02	0.018	10.32	0.106	-	-	5.74	0.017	0
S003	0.47075	0.80536	-	-	-	-	-	-	-	-	7.22	0.038	0
S004	0.39334	0.81997	-	-	7.73	0.017	7.09	0.023	7.06	0.023	6.96	0.024	0
S005	0.45670	0.82530	12.26	0.020	11.13	0.019	8.34	0.025	6.64	0.026	5.61	0.018	0
S006	0.45925	0.82758	-	-	11.60	0.022	10.65	0.117	-	-	4.42	0.013	0
S007	0.41950	0.85478	-	-	12.60	0.032	-	-	-	-	5.79	0.014	0
S008	0.40562	0.85646	11.48	0.019	10.96	0.019	9.91	0.092	9.01	0.204	7.18	0.036	0
S009	0.39960	0.86690	-	-	-	-	-	-	9.37	0.544	5.87	0.018	4
S010	0.46682	0.87328	-	-	-	-	-	-	-	-	6.05	0.018	0
S011	0.40107	0.87249	-	-	-	-	-	-	-	-	7.29	0.044	0
S012	0.43994	0.82226	-	-	-	-	-	-	-	-	8.35	0.542	5
S013	0.41968	0.84852	12.11	0.020	11.42	0.020	9.74	0.054	-	-	7.61	0.109	5
S014	0.42627	0.83972	12.43	0.020	11.81	0.021	10.54	0.086	9.01	0.086	8.93	0.110	5
S015	0.44958	0.82222	15.17	0.102	13.76	0.088	-	-	-	-	9.33	0.543	5
S016	0.46143	0.79103	-	-	-	-	-	-	-	-	7.96	0.109	5
S017	0.45306	0.85042	10.38	0.018	8.04	0.017	7.68	0.020	7.64	0.029	8.46	0.109	5
S018	0.45019	0.85680	9.43	0.022	9.11	0.020	6.96	0.018	6.77	0.022	7.93	0.109	5
S019	0.45602	0.86614	-	-	7.61	0.020	-	-	7.38	0.027	7.84	0.109	5
S020	0.42007	0.87652	-	-	-	-	-	-	-	-	7.39	0.109	5
S021	0.39506	0.80320	8.54	0.018	8.55	0.017	8.11	0.021	7.81	0.033	-	-	0
S022	0.39978	0.79872	-	-	-	-	-	-	9.28	0.101	-	-	0
S023	0.40124	0.79863	-	-	-	-	10.93	0.108	9.33	0.101	-	-	0
S024	0.39246	0.82750	11.87	0.020	11.84	0.023	10.55	0.093	9.55	0.143	-	-	0
S025	0.38947	0.84212	10.06	0.019	10.04	0.017	8.61	0.020	9.23	0.083	-	-	0
S026	0.39586	0.82203	10.24	0.018	10.29	0.018	9.64	0.043	9.33	0.116	-	-	0
S027	0.40703	0.78927	9.21	0.017	9.45	0.018	8.70	0.024	8.62	0.056	-	-	0
S028	0.38666	0.86991	-	-	10.49	0.019	-	-	9.29	0.138	-	-	0
S029	0.39918	0.84336	-	-	-	-	11.27	0.160	9.63	0.170	-	-	0
S030	0.41152	0.80173	-	-	-	-	10.67	0.093	9.16	0.098	-	-	0
S031	0.41147	0.80394	-	-	-	-	11.09	0.134	9.29	0.105	-	-	0
S032	0.41371	0.80306	-	-	-	-	11.09	0.139	9.60	0.147	-	-	0
S033	0.41585	0.78976	9.99	0.022	9.18	0.017	8.58	0.022	8.52	0.051	-	-	0
S034	0.39724	0.85564	-	-	-	-	-	-	9.71	0.209	-	-	0
S035	0.39691	0.85729	-	-	-	-	-	-	9.44	0.201	-	-	0
S036	0.39825	0.85835	14.05	0.050	13.45	0.065	11.03	0.212	9.11	0.163	-	-	0
S037	0.39986	0.85800	-	-	-	-	-	-	9.21	0.199	-	-	0
S038	0.40324	0.84294	13.32	0.028	13.12	0.049	11.27	0.194	9.61	0.196	-	-	0
S039	0.41507	0.79818	14.30	0.045	13.91	0.074	11.17	0.155	9.62	0.167	-	-	0
S040	0.42033	0.78008	10.29	0.018	10.50	0.018	8.97	0.024	9.46	0.115	-	-	0
S041	0.41549	0.80570	13.07	0.024	-	-	11.32	0.210	9.38	0.133	-	-	0
S042	0.40682	0.83704	-	-	13.78	0.078	11.29	0.175	9.62	0.167	-	-	0
S043	0.40823	0.83762	-	-	-	-	11.24	0.188	9.56	0.174	-	-	0
S044	0.41766	0.79905	-	-	-	-	-	-	9.80	0.205	-	-	0
S045	0.41424	0.81540	11.49	0.018	11.54	0.020	10.70	0.096	10.04	0.214	-	-	0
S046	0.41533	0.81400	12.84	0.023	12.63	0.030	10.90	0.110	9.67	0.155	-	-	0
S047	0.41667	0.81398	-	-	-	-	-	-	9.61	0.144	-	-	0
S048	0.41803	0.81389	11.95	0.019	11.97	0.022	10.48	0.077	9.51	0.135	-	-	0
S049	0.41876	0.81570	-	-	-	-	-	-	9.72	0.166	-	-	0
S050	0.41947	0.80390	-	-	-	-	11.16	0.154	9.51	0.166	-	-	0
S051	0.40875	0.85004	10.35	0.018	10.53	0.018	9.84	0.068	9.26	0.178	-	-	0
S052	0.41362	0.83715	-	-	-	-	-	-	9.39	0.185	-	-	0
S053	0.41976	0.81959	-	-	-	-	11.28	0.187	9.76	0.207	-	-	0
S054	0.42220	0.81237	-	-	-	-	-	-	9.85	0.205	-	-	0
S055	0.41500	0.85281	12.76	0.068	9.66	0.017	8.12	0.022	8.41	0.091	-	-	0
S056	0.43658	0.78834	11.51	0.021	11.07	0.019	10.02	0.043	9.44	0.094	-	-	0
S057	0.41915	0.85928	9.89	0.017	9.96	0.018	9.45	0.047	9.16	0.169	-	-	0
S058	0.43516	0.81068	10.46	0.024	9.78	0.017	9.25	0.029	8.99	0.069	-	-	0
S059	0.43856	0.80048	-	-	-	-	11.20	0.122	9.73	0.133	-	-	0
S060	0.43898	0.79906	-	-	-	-	11.40	0.150	9.87	0.152	-	-	0

continued on next page ...

Table 4. The complete list of merged point sources, continued.

name	RA -290 (degrees)	Dec. -13 (degrees)	[3.6] (mag)	$\sigma_{[3.6]}$ (mag)	[4.5] (mag)	$\sigma_{[4.5]}$ (mag)	[5.8] (mag)	$\sigma_{[5.8]}$ (mag)	[8.0] (mag)	$\sigma_{[8.0]}$ (mag)	[24] (mag)	$\sigma_{[24]}$ (mag)	ap. phot. flag
S061	0.44033	0.79966	-	-	-	-	11.47	0.152	9.63	0.110	-	-	0
S062	0.44287	0.79545	10.43	0.018	10.56	0.018	10.88	0.093	9.18	0.069	-	-	0
S063	0.43977	0.80598	10.42	0.017	10.69	0.018	9.35	0.029	9.89	0.157	-	-	0
S064	0.43300	0.83343	10.07	0.017	10.18	0.017	9.54	0.041	9.45	0.154	-	-	0
S065	0.44362	0.80272	-	-	-	-	-	-	10.08	0.175	-	-	0
S066	0.43314	0.85563	-	-	-	-	10.99	0.128	9.49	0.150	-	-	0
S067	0.43561	0.85211	8.51	0.017	8.57	0.017	8.26	0.020	8.16	0.041	-	-	0
S068	0.43346	0.86044	-	-	-	-	-	-	9.38	0.116	-	-	0
S069	0.43418	0.85683	-	-	-	-	-	-	9.39	0.130	-	-	0
S070	0.45191	0.79754	10.29	0.018	10.42	0.018	9.53	0.042	9.13	0.117	-	-	0
S071	0.43899	0.85464	-	-	-	-	-	-	9.85	0.206	-	-	0
S072	0.45369	0.82115	9.45	0.017	9.64	0.018	8.92	0.036	8.81	0.147	-	-	0
S073	0.45417	0.82186	9.30	0.017	9.65	0.018	9.07	0.041	9.20	0.204	-	-	0
S074	0.46180	0.79902	-	-	-	-	10.85	0.164	9.09	0.143	-	-	0
S075	0.45905	0.80223	11.35	0.018	11.12	0.019	10.25	0.099	9.35	0.187	-	-	0
S076	0.44891	0.83812	12.46	0.021	12.36	0.026	10.84	0.092	9.62	0.133	-	-	0
S077	0.45228	0.83354	-	-	-	-	-	-	9.62	0.150	-	-	0
S078	0.45095	0.83633	10.21	0.017	10.43	0.017	9.75	0.039	9.27	0.103	-	-	0
S079	0.44358	0.86791	9.49	0.018	9.77	0.018	9.27	0.030	8.83	0.074	-	-	0
S080	0.44798	0.85537	13.14	0.031	12.82	0.056	10.93	0.131	9.63	0.159	-	-	0
S081	0.45283	0.83721	12.12	0.020	11.88	0.022	10.48	0.070	9.53	0.117	-	-	0
S082	0.46007	0.83104	11.97	0.019	11.28	0.019	10.27	0.071	9.84	0.195	-	-	0
S083	0.46577	0.81531	13.84	0.032	-	-	-	-	10.06	0.206	-	-	0
S084	0.47115	0.79349	12.83	0.022	12.80	0.031	11.01	0.121	9.80	0.165	-	-	0
S085	0.46364	0.82875	-	-	-	-	-	-	9.98	0.221	-	-	0
S086	0.46382	0.83289	15.53	0.135	-	-	11.72	0.220	9.95	0.170	-	-	0
S087	0.46306	0.84244	13.09	0.028	12.73	0.036	-	-	10.07	0.182	-	-	0
S088	0.46463	0.84146	9.94	0.017	10.14	0.017	8.54	0.020	8.56	0.048	-	-	0
S089	0.47436	0.80855	-	-	-	-	-	-	9.81	0.169	-	-	0
S090	0.46320	0.84980	12.75	0.024	12.56	0.034	11.60	0.201	9.84	0.167	-	-	0
S091	0.46048	0.86229	9.91	0.018	10.17	0.018	9.76	0.042	8.18	0.041	-	-	0
S092	0.47075	0.82999	11.35	0.019	11.39	0.027	9.70	0.035	9.76	0.128	-	-	0
S093	0.47348	0.82603	16.00	2.014	9.05	0.017	8.43	0.020	8.42	0.041	-	-	0
S094	0.48126	0.79919	-	-	13.41	0.072	-	-	9.71	0.176	-	-	0
S095	0.48048	0.80019	-	-	14.06	0.083	-	-	9.82	0.183	-	-	0
S096	0.47737	0.81129	-	-	-	-	-	-	9.63	0.148	-	-	0
S097	0.47834	0.81255	12.24	0.020	12.24	0.024	10.79	0.091	9.58	0.135	-	-	0
S098	0.47747	0.81364	11.41	0.018	11.47	0.020	-	-	9.97	0.200	-	-	0
S099	0.48442	0.79537	10.69	0.018	10.82	0.019	9.90	0.061	9.28	0.162	-	-	0
S100	0.47676	0.82397	12.62	0.037	11.40	0.020	10.46	0.061	10.42	0.235	-	-	0
S101	0.46922	0.85257	10.24	0.018	10.42	0.019	9.62	0.047	9.09	0.113	-	-	0
S102	0.46766	0.86023	-	-	-	-	11.31	0.188	9.55	0.153	-	-	0
S103	0.46743	0.86805	10.63	0.023	10.15	0.019	9.68	0.053	9.05	0.117	-	-	0
S104	0.47068	0.86468	10.03	0.019	10.32	0.020	9.44	0.044	8.89	0.098	-	-	0
S105	0.47726	0.86360	-	-	-	-	-	-	9.66	0.110	-	-	4
S106	0.45755	0.85238	10.63	0.018	10.74	0.019	10.23	0.065	10.85	0.110	-	-	4
S107	0.43640	0.87763	-	-	-	-	-	-	8.93	0.110	-	-	4
S108	0.42157	0.87883	-	-	8.65	0.018	-	-	8.69	0.542	-	-	4
S109	0.42157	0.87883	-	-	8.65	0.018	-	-	9.37	0.109	-	-	4
S110	0.40909	0.86113	11.15	0.027	9.64	0.018	8.97	0.049	8.88	0.110	-	-	4
S111	0.39221	0.86985	-	-	-	-	-	-	9.62	0.110	-	-	4
S112	0.40781	0.84516	11.41	0.018	11.37	0.020	10.76	0.140	11.34	0.543	-	-	4
S113	0.44269	0.84368	11.65	0.020	11.23	0.019	10.29	0.051	10.42	0.110	-	-	4
S114	0.45947	0.81791	11.14	0.018	10.93	0.018	10.07	0.071	10.81	0.110	-	-	4
S115	0.38844	0.81691	13.63	0.064	13.41	0.097	-	-	-	-	-	-	0
S116	0.38838	0.81728	13.39	0.057	12.33	0.041	-	-	-	-	-	-	0
S117	0.38435	0.83560	13.24	0.037	12.50	0.031	11.80	0.236	-	-	-	-	0
S118	0.39744	0.80177	12.33	0.023	12.22	0.028	10.93	0.113	-	-	-	-	0
S119	0.39520	0.80606	13.35	0.030	12.95	0.038	-	-	-	-	-	-	0
S120	0.39630	0.79560	11.80	0.022	12.09	0.028	10.64	0.100	-	-	-	-	0
S121	0.39211	0.81406	12.64	0.027	12.10	0.029	-	-	-	-	-	-	0
S122	0.38790	0.82988	11.31	0.020	11.45	0.022	9.77	0.044	-	-	-	-	0
S123	0.39807	0.79416	11.33	0.020	11.50	0.021	9.63	0.040	-	-	-	-	0
S124	0.39658	0.80018	13.43	0.033	13.18	0.049	-	-	-	-	-	-	0
S125	0.39587	0.81984	12.77	0.024	12.55	0.032	-	-	-	-	-	-	0

continued on next page ...

Table 4. The complete list of merged point sources, continued.

name	RA -290 (degrees)	Dec. -13 (degrees)	[3.6] (mag)	$\sigma_{[3.6]}$ (mag)	[4.5] (mag)	$\sigma_{[4.5]}$ (mag)	[5.8] (mag)	$\sigma_{[5.8]}$ (mag)	[8.0] (mag)	$\sigma_{[8.0]}$ (mag)	[24] (mag)	$\sigma_{[24]}$ (mag)	ap. phot. flag
S126	0.39432	0.81740	13.38	0.032	13.07	0.050	-	-	-	-	-	-	0
S127	0.39101	0.82317	11.92	0.021	11.87	0.027	-	-	-	-	-	-	0
S128	0.38733	0.83615	12.48	0.024	12.35	0.027	-	-	-	-	-	-	0
S129	0.39369	0.81309	12.43	0.023	12.18	0.027	10.70	0.084	-	-	-	-	0
S130	0.38607	0.84332	13.58	0.039	13.38	0.057	-	-	-	-	-	-	0
S131	0.38654	0.84291	12.88	0.029	12.90	0.041	-	-	-	-	-	-	0
S132	0.39585	0.80815	14.33	0.055	13.94	0.088	-	-	-	-	-	-	0
S133	0.38541	0.85500	11.80	0.020	11.75	0.022	11.19	0.118	-	-	-	-	0
S134	0.38693	0.84802	14.36	0.052	13.94	0.077	-	-	-	-	-	-	0
S135	0.39168	0.83462	15.73	0.151	14.78	0.177	-	-	-	-	-	-	0
S136	0.39081	0.83458	13.88	0.035	13.67	0.058	-	-	-	-	-	-	0
S137	0.40667	0.77423	13.24	0.035	12.39	0.028	-	-	-	-	-	-	0
S138	0.38907	0.84469	13.29	0.028	12.92	0.036	-	-	-	-	-	-	0
S139	0.38606	0.85692	12.12	0.024	11.99	0.024	10.76	0.091	-	-	-	-	0
S140	0.39374	0.82879	13.36	0.031	13.22	0.051	-	-	-	-	-	-	0
S141	0.40596	0.78660	13.90	0.038	13.56	0.056	-	-	-	-	-	-	0
S142	0.40219	0.80157	13.12	0.029	12.74	0.033	-	-	-	-	-	-	0
S143	0.39875	0.81619	14.24	0.050	14.34	0.126	-	-	-	-	-	-	0
S144	0.39848	0.81679	13.62	0.034	13.37	0.057	-	-	-	-	-	-	0
S145	0.40061	0.80844	14.62	0.061	14.39	0.116	-	-	-	-	-	-	0
S146	0.39999	0.81197	13.70	0.038	13.47	0.055	-	-	-	-	-	-	0
S147	0.40922	0.78928	13.03	0.025	13.00	0.039	-	-	-	-	-	-	0
S148	0.40203	0.80483	13.79	0.040	13.05	0.040	-	-	-	-	-	-	0
S149	0.39066	0.85022	13.09	0.026	13.07	0.041	-	-	-	-	-	-	0
S150	0.40030	0.81796	11.81	0.020	11.77	0.022	11.77	0.225	-	-	-	-	0
S151	0.39436	0.84012	13.89	0.038	13.27	0.046	-	-	-	-	-	-	0
S152	0.40375	0.80661	13.29	0.027	13.33	0.049	-	-	-	-	-	-	0
S153	0.41158	0.77953	11.93	0.020	12.01	0.023	11.21	0.122	-	-	-	-	0
S154	0.39734	0.83434	14.61	0.062	14.21	0.104	-	-	-	-	-	-	0
S155	0.39274	0.85321	12.87	0.025	12.72	0.034	-	-	-	-	-	-	0
S156	0.40426	0.80985	13.36	0.027	13.19	0.041	-	-	-	-	-	-	0
S157	0.40625	0.80258	11.96	0.020	12.08	0.023	-	-	-	-	-	-	0
S158	0.39962	0.82858	12.29	0.022	12.08	0.025	10.91	0.112	-	-	-	-	0
S159	0.40114	0.82917	14.52	0.067	13.71	0.073	-	-	-	-	-	-	0
S160	0.40287	0.82879	10.76	0.018	10.93	0.019	10.28	0.062	-	-	-	-	0
S161	0.40405	0.83025	13.44	0.028	13.40	0.053	-	-	-	-	-	-	0
S162	0.40139	0.82699	13.27	0.029	12.70	0.033	-	-	-	-	-	-	0
S163	0.39397	0.85201	14.22	0.052	13.34	0.051	-	-	-	-	-	-	0
S164	0.40808	0.79803	12.84	0.027	12.85	0.032	-	-	-	-	-	-	0
S165	0.39991	0.83102	11.50	0.019	11.57	0.021	9.95	0.048	-	-	-	-	0
S166	0.41034	0.79365	10.66	0.018	10.81	0.018	10.16	0.055	-	-	-	-	0
S167	0.41134	0.79401	12.38	0.022	12.33	0.028	-	-	-	-	-	-	0
S168	0.39988	0.83311	14.44	0.089	12.09	0.024	11.24	0.147	-	-	-	-	0
S169	0.39615	0.84856	11.48	0.020	11.43	0.020	10.69	0.091	-	-	-	-	0
S170	0.39440	0.85395	13.76	0.038	13.43	0.055	-	-	-	-	-	-	0
S171	0.39501	0.85376	12.76	0.024	12.79	0.035	-	-	-	-	-	-	0
S172	0.39984	0.83588	13.35	0.030	12.69	0.031	-	-	-	-	-	-	0
S173	0.41311	0.78390	13.87	0.041	13.54	0.063	-	-	-	-	-	-	0
S174	0.40928	0.79977	12.64	0.024	12.21	0.024	11.00	0.118	-	-	-	-	0
S175	0.40385	0.82019	13.67	0.031	13.65	0.055	-	-	-	-	-	-	0
S176	0.39429	0.85746	12.48	0.023	12.33	0.027	11.34	0.177	-	-	-	-	0
S177	0.40630	0.81155	13.73	0.033	13.78	0.063	-	-	-	-	-	-	0
S178	0.40426	0.82290	13.78	0.036	13.48	0.055	-	-	-	-	-	-	0
S179	0.40351	0.82337	12.97	0.024	12.93	0.035	-	-	-	-	-	-	0
S180	0.41397	0.78223	13.20	0.028	13.22	0.049	-	-	-	-	-	-	0
S181	0.41195	0.79080	12.91	0.026	12.63	0.033	-	-	-	-	-	-	0
S182	0.41590	0.77713	11.78	0.021	11.94	0.025	10.64	0.085	-	-	-	-	0
S183	0.40788	0.80783	13.89	0.044	13.85	0.079	-	-	-	-	-	-	0
S184	0.40641	0.81394	-	-	12.90	0.035	11.20	0.116	9.86	0.140	-	-	0
S185	0.39937	0.84181	13.25	0.030	12.92	0.037	-	-	-	-	-	-	0
S186	0.41178	0.79594	11.94	0.020	11.93	0.023	10.91	0.113	-	-	-	-	0
S187	0.41198	0.79759	12.54	0.025	12.52	0.028	11.30	0.162	-	-	-	-	0
S188	0.40521	0.82031	13.61	0.030	13.55	0.051	-	-	-	-	-	-	0
S189	0.40891	0.81021	12.10	0.019	12.04	0.022	11.33	0.147	-	-	-	-	0
S190	0.41019	0.80962	12.76	0.027	12.55	0.029	-	-	-	-	-	-	0

continued on next page ...

Table 4. The complete list of merged point sources, continued.

name	RA -290 (degrees)	Dec. -13 (degrees)	[3.6] (mag)	$\sigma_{[3.6]}$ (mag)	[4.5] (mag)	$\sigma_{[4.5]}$ (mag)	[5.8] (mag)	$\sigma_{[5.8]}$ (mag)	[8.0] (mag)	$\sigma_{[8.0]}$ (mag)	[24] (mag)	$\sigma_{[24]}$ (mag)	ap. phot. flag
S191	0.41525	0.78694	12.58	0.022	12.67	0.033	-	-	-	-	-	-	0
S192	0.40634	0.82137	14.10	0.049	13.55	0.047	-	-	-	-	-	-	0
S193	0.40793	0.81582	12.93	0.022	12.85	0.030	11.80	0.212	-	-	-	-	0
S194	0.40335	0.83629	11.51	0.018	11.56	0.020	10.43	0.072	-	-	-	-	0
S195	0.40269	0.83845	11.64	0.019	11.66	0.020	10.74	0.104	-	-	-	-	0
S196	0.40635	0.82924	12.27	0.022	12.03	0.023	-	-	-	-	-	-	0
S197	0.42137	0.77387	11.44	0.021	11.41	0.024	-	-	-	-	-	-	0
S198	0.42023	0.77797	12.27	0.021	12.71	0.038	10.82	0.104	-	-	-	-	0
S199	0.40214	0.84836	13.98	0.046	13.45	0.062	-	-	-	-	-	-	0
S200	0.41631	0.79453	13.29	0.029	13.29	0.052	-	-	-	-	-	-	0
S201	0.40206	0.85228	13.22	0.028	12.95	0.041	-	-	-	-	-	-	0
S202	0.40236	0.85392	13.32	0.029	13.03	0.044	-	-	-	-	-	-	0
S203	0.42041	0.78801	12.04	0.022	11.74	0.021	11.29	0.134	-	-	-	-	0
S204	0.40974	0.82844	13.81	0.033	13.42	0.045	11.54	0.179	-	-	-	-	0
S205	0.41114	0.82565	13.35	0.025	13.11	0.034	11.12	0.133	-	-	-	-	0
S206	0.41189	0.82658	13.01	0.022	12.82	0.029	-	-	-	-	-	-	0
S207	0.41592	0.80785	13.91	0.037	13.71	0.069	-	-	-	-	-	-	0
S208	0.40538	0.85141	13.65	0.036	13.06	0.043	-	-	-	-	-	-	0
S209	0.40441	0.85612	11.89	0.020	11.80	0.023	-	-	-	-	-	-	0
S210	0.40400	0.85768	14.06	0.047	13.93	0.106	-	-	-	-	-	-	0
S211	0.40261	0.86130	14.04	0.051	13.91	0.110	-	-	-	-	-	-	0
S212	0.42164	0.78989	13.56	0.031	13.49	0.053	-	-	-	-	-	-	0
S213	0.42107	0.79069	13.69	0.033	13.48	0.058	-	-	-	-	-	-	0
S214	0.41180	0.82870	14.05	0.038	14.10	0.080	-	-	-	-	-	-	0
S215	0.41172	0.82834	14.13	0.039	13.84	0.063	-	-	-	-	-	-	0
S216	0.40726	0.84647	14.28	0.054	14.66	0.171	-	-	-	-	-	-	0
S217	0.41125	0.83214	13.88	0.035	13.84	0.076	-	-	-	-	-	-	0
S218	0.42522	0.78039	12.28	0.021	12.19	0.025	11.74	0.235	-	-	-	-	0
S219	0.41396	0.82560	13.59	0.028	13.30	0.042	-	-	-	-	-	-	0
S220	0.42194	0.79553	12.06	0.019	12.15	0.023	-	-	-	-	-	-	0
S221	0.42228	0.79399	14.66	0.060	14.21	0.088	-	-	-	-	-	-	0
S222	0.42029	0.80153	14.14	0.042	14.20	0.088	-	-	-	-	-	-	0
S223	0.42659	0.77769	13.00	0.027	12.89	0.042	-	-	-	-	-	-	0
S224	0.42773	0.77791	11.51	0.020	11.58	0.023	10.45	0.077	-	-	-	-	0
S225	0.41768	0.81598	14.04	0.037	13.62	0.056	-	-	-	-	-	-	0
S226	0.42082	0.80311	13.94	0.040	12.86	0.033	-	-	-	-	-	-	0
S227	0.41872	0.80980	13.29	0.027	13.21	0.044	-	-	-	-	-	-	0
S228	0.40786	0.85393	14.21	0.054	13.60	0.074	-	-	-	-	-	-	0
S229	0.41078	0.84600	11.04	0.018	11.18	0.019	10.56	0.117	-	-	-	-	0
S230	0.42449	0.79091	14.15	0.044	13.96	0.076	-	-	-	-	-	-	0
S231	0.42271	0.79927	13.97	0.036	13.92	0.070	-	-	-	-	-	-	0
S232	0.42290	0.79964	13.46	0.027	13.38	0.045	-	-	-	-	-	-	0
S233	0.41308	0.83930	12.55	0.021	12.45	0.029	10.71	0.140	-	-	-	-	0
S234	0.41409	0.84090	11.46	0.018	11.62	0.021	10.51	0.124	-	-	-	-	0
S235	0.40694	0.86180	14.05	0.052	13.73	0.103	-	-	-	-	-	-	0
S236	0.41272	0.84332	14.72	0.080	14.35	0.134	-	-	-	-	-	-	0
S237	0.42601	0.79279	15.60	0.140	14.00	0.074	-	-	-	-	-	-	0
S238	0.42932	0.78226	13.44	0.039	12.32	0.025	-	-	-	-	-	-	0
S239	0.42048	0.81503	-	-	14.09	0.105	11.29	0.159	-	-	-	-	0
S240	0.42111	0.81437	13.36	0.027	13.07	0.039	-	-	-	-	-	-	0
S241	0.41505	0.83837	12.86	0.023	12.66	0.033	-	-	-	-	-	-	0
S242	0.42566	0.79926	14.66	0.062	13.55	0.047	11.74	0.221	-	-	-	-	0
S243	0.41847	0.82814	12.66	0.021	12.60	0.030	-	-	-	-	-	-	0
S244	0.41871	0.82960	11.58	0.018	11.65	0.020	-	-	-	-	-	-	0
S245	0.42015	0.82776	11.83	0.018	11.71	0.021	-	-	-	-	-	-	0
S246	0.41713	0.82981	13.63	0.033	13.47	0.054	-	-	-	-	-	-	0
S247	0.43170	0.77736	12.13	0.023	11.92	0.025	10.79	0.097	-	-	-	-	0
S248	0.41535	0.84444	14.07	0.047	13.57	0.068	-	-	-	-	-	-	0
S249	0.42169	0.81943	13.80	0.032	13.68	0.062	-	-	-	-	-	-	0
S250	0.41703	0.83590	14.29	0.055	13.66	0.065	-	-	-	-	-	-	0
S251	0.42818	0.79450	14.09	0.037	13.90	0.063	-	-	-	-	-	-	0
S252	0.41604	0.84732	12.77	0.023	12.64	0.035	-	-	-	-	-	-	0
S253	0.43249	0.78840	11.52	0.019	11.60	0.020	10.61	0.074	-	-	-	-	0
S254	0.42400	0.82271	13.72	0.030	13.53	0.059	-	-	-	-	-	-	0
S255	0.42480	0.82357	12.36	0.019	12.12	0.024	10.70	0.131	-	-	-	-	0

continued on next page ...

Table 4. The complete list of merged point sources, continued.

name	RA -290 (degrees)	Dec. -13 (degrees)	[3.6] (mag)	$\sigma_{[3.6]}$ (mag)	[4.5] (mag)	$\sigma_{[4.5]}$ (mag)	[5.8] (mag)	$\sigma_{[5.8]}$ (mag)	[8.0] (mag)	$\sigma_{[8.0]}$ (mag)	[24] (mag)	$\sigma_{[24]}$ (mag)	ap. phot. flag
S256	0.43034	0.79762	13.63	0.028	13.52	0.044	-	-	-	-	-	-	0
S257	0.42728	0.81191	13.98	0.034	14.07	0.082	-	-	-	-	-	-	0
S258	0.41438	0.85976	14.26	0.057	13.68	0.089	-	-	-	-	-	-	0
S259	0.41544	0.85887	14.81	0.085	14.32	0.158	-	-	-	-	-	-	0
S260	0.41926	0.84627	14.28	0.055	13.71	0.065	-	-	-	-	-	-	0
S261	0.42279	0.83587	13.62	0.037	13.55	0.068	-	-	-	-	-	-	0
S262	0.41726	0.85677	12.88	0.025	12.61	0.035	10.52	0.119	-	-	-	-	0
S263	0.41553	0.86282	13.39	0.034	12.45	0.036	-	-	-	-	-	-	0
S264	0.43726	0.77800	13.78	0.048	13.83	0.082	-	-	-	-	-	-	0
S265	0.43770	0.77764	13.23	0.034	12.90	0.043	-	-	-	-	-	-	0
S266	0.43716	0.78297	13.40	0.029	13.35	0.049	-	-	-	-	-	-	0
S267	0.43571	0.79239	11.39	0.019	11.54	0.020	10.37	0.064	-	-	-	-	0
S268	0.42282	0.84598	13.55	0.029	13.06	0.037	-	-	-	-	-	-	0
S269	0.42360	0.84725	12.20	0.020	12.11	0.023	11.45	0.218	-	-	-	-	0
S270	0.43841	0.78477	13.98	0.040	13.78	0.068	-	-	-	-	-	-	0
S271	0.43259	0.80702	13.38	0.026	13.55	0.053	-	-	-	-	-	-	0
S272	0.42863	0.82395	15.20	0.080	13.92	0.075	-	-	-	-	-	-	0
S273	0.42747	0.82929	15.00	0.080	14.58	0.159	-	-	-	-	-	-	0
S274	0.42874	0.82960	15.14	0.091	14.69	0.174	-	-	-	-	-	-	0
S275	0.43373	0.80542	12.75	0.023	12.40	0.025	-	-	-	-	-	-	0
S276	0.42712	0.83240	12.63	0.022	12.29	0.027	11.02	0.188	-	-	-	-	0
S277	0.42351	0.84330	13.94	0.038	13.67	0.062	-	-	-	-	-	-	0
S278	0.44018	0.77995	13.86	0.044	13.49	0.055	-	-	-	-	-	-	0
S279	0.43973	0.78342	10.73	0.018	10.79	0.018	-	-	-	-	-	-	0
S280	0.43280	0.80999	13.33	0.025	13.13	0.038	-	-	-	-	-	-	0
S281	0.43682	0.79707	13.01	0.022	12.86	0.031	-	-	-	-	-	-	0
S282	0.42759	0.83876	13.67	0.032	13.50	0.056	-	-	-	-	-	-	0
S283	0.41936	0.86450	13.28	0.033	13.16	0.056	-	-	-	-	-	-	0
S284	0.43979	0.78737	12.11	0.020	12.13	0.024	11.25	0.119	-	-	-	-	0
S285	0.44132	0.78780	11.44	0.019	11.49	0.020	10.90	0.091	-	-	-	-	0
S286	0.43990	0.78901	11.87	0.020	11.82	0.022	10.94	0.084	-	-	-	-	0
S287	0.43098	0.82118	15.03	0.065	14.13	0.087	-	-	-	-	-	-	0
S288	0.43883	0.79449	14.02	0.040	13.90	0.069	-	-	-	-	-	-	0
S289	0.43835	0.79401	14.28	0.047	14.11	0.084	-	-	-	-	-	-	0
S290	0.42778	0.83649	13.36	0.028	13.31	0.055	-	-	-	-	-	-	0
S291	0.44066	0.79140	13.08	0.042	11.80	0.022	11.09	0.108	-	-	-	-	0
S292	0.43357	0.81957	14.67	0.051	14.15	0.095	-	-	-	-	-	-	0
S293	0.44426	0.78066	14.42	0.074	13.39	0.056	-	-	-	-	-	-	0
S294	0.43892	0.80308	13.48	0.027	13.63	0.055	-	-	-	-	-	-	0
S295	0.43063	0.83516	11.63	0.018	11.67	0.021	11.08	0.149	-	-	-	-	0
S296	0.42399	0.85934	14.00	0.039	14.12	0.096	-	-	-	-	-	-	0
S297	0.42360	0.86145	13.11	0.026	13.06	0.042	-	-	-	-	-	-	0
S298	0.44421	0.78217	13.65	0.043	12.66	0.034	-	-	-	-	-	-	0
S299	0.43830	0.80643	13.20	0.024	12.95	0.033	-	-	-	-	-	-	0
S300	0.43152	0.83376	14.08	0.041	13.82	0.078	-	-	-	-	-	-	0
S301	0.43410	0.83267	13.07	0.025	12.93	0.039	-	-	-	-	-	-	0
S302	0.43264	0.83157	13.46	0.031	13.26	0.052	-	-	-	-	-	-	0
S303	0.42361	0.86548	13.42	0.035	13.07	0.047	-	-	-	-	-	-	0
S304	0.43631	0.81874	12.81	0.021	12.57	0.029	-	-	-	-	-	-	0
S305	0.43083	0.84064	13.98	0.051	12.84	0.034	11.44	0.145	-	-	-	-	0
S306	0.42679	0.85524	14.02	0.045	13.58	0.059	-	-	-	-	-	-	0
S307	0.42533	0.86228	12.52	0.029	11.74	0.021	10.47	0.076	-	-	-	-	0
S308	0.43832	0.81410	13.68	0.028	13.36	0.046	-	-	-	-	-	-	0
S309	0.43915	0.81499	13.94	0.032	13.73	0.061	-	-	-	-	-	-	0
S310	0.42843	0.85236	13.12	0.031	12.92	0.035	-	-	-	-	-	-	0
S311	0.42690	0.85786	13.66	0.034	13.41	0.049	-	-	-	-	-	-	0
S312	0.42889	0.85417	13.39	0.029	13.27	0.048	-	-	-	-	-	-	0
S313	0.44723	0.78439	13.37	0.028	13.35	0.052	-	-	-	-	-	-	0
S314	0.44091	0.81009	14.31	0.046	14.13	0.090	-	-	-	-	-	-	0
S315	0.43737	0.82637	14.15	0.039	14.20	0.109	10.96	0.179	-	-	-	-	0
S316	0.43486	0.83549	11.35	0.018	11.43	0.019	10.85	0.093	-	-	-	-	0
S317	0.43621	0.83507	12.99	0.023	12.79	0.032	-	-	-	-	-	-	0
S318	0.44197	0.80934	13.52	0.028	13.52	0.054	-	-	-	-	-	-	0
S319	0.44832	0.78681	12.44	0.021	12.40	0.027	10.65	0.072	-	-	-	-	0
S320	0.44209	0.81316	12.57	0.020	12.54	0.028	11.18	0.167	-	-	-	-	0

continued on next page ...

Table 4. The complete list of merged point sources, continued.

name	RA -290 (degrees)	Dec. -13 (degrees)	[3.6] (mag)	$\sigma_{[3.6]}$ (mag)	[4.5] (mag)	$\sigma_{[4.5]}$ (mag)	[5.8] (mag)	$\sigma_{[5.8]}$ (mag)	[8.0] (mag)	$\sigma_{[8.0]}$ (mag)	[24] (mag)	$\sigma_{[24]}$ (mag)	ap. phot. flag
S321	0.43909	0.82623	14.31	0.050	13.41	0.053	10.80	0.152	-	-	-	-	0
S322	0.43872	0.82818	13.70	0.031	13.33	0.050	-	-	-	-	-	-	0
S323	0.44018	0.82780	13.67	0.034	13.52	0.059	-	-	-	-	-	-	0
S324	0.45037	0.78070	11.60	0.021	11.71	0.025	-	-	-	-	-	-	0
S325	0.44712	0.79132	14.01	0.041	13.79	0.071	-	-	-	-	-	-	0
S326	0.44396	0.80545	12.98	0.022	12.84	0.031	-	-	-	-	-	-	0
S327	0.44114	0.81462	14.35	0.043	14.01	0.081	-	-	-	-	-	-	0
S328	0.44121	0.81730	14.12	0.038	13.57	0.058	-	-	-	-	-	-	0
S329	0.43357	0.85007	12.48	0.021	12.23	0.026	11.35	0.150	-	-	-	-	0
S330	0.43704	0.85006	12.83	0.023	12.72	0.038	-	-	-	-	-	-	0
S331	0.43772	0.83250	12.33	0.021	12.07	0.023	11.57	0.185	-	-	-	-	0
S332	0.43251	0.85140	13.06	0.025	13.19	0.051	-	-	-	-	-	-	0
S333	0.45095	0.78331	10.77	0.019	10.85	0.020	10.19	0.063	-	-	-	-	0
S334	0.44768	0.79703	12.93	0.025	12.79	0.032	11.35	0.138	-	-	-	-	0
S335	0.44881	0.79902	12.37	0.023	11.93	0.022	11.63	0.204	-	-	-	-	0
S336	0.44519	0.80766	13.80	0.034	13.75	0.060	-	-	-	-	-	-	0
S337	0.44449	0.80768	13.98	0.039	13.61	0.056	-	-	-	-	-	-	0
S338	0.43773	0.83792	13.43	0.032	12.67	0.031	-	-	-	-	-	-	0
S339	0.43260	0.86131	12.64	0.025	12.45	0.028	10.83	0.103	-	-	-	-	0
S340	0.44672	0.80430	12.50	0.020	12.32	0.025	-	-	-	-	-	-	0
S341	0.43664	0.84347	12.82	0.024	12.72	0.031	-	-	-	-	-	-	0
S342	0.43274	0.85896	14.02	0.042	13.84	0.073	-	-	-	-	-	-	0
S343	0.44183	0.82532	12.28	0.020	12.29	0.027	10.58	0.136	-	-	-	-	0
S344	0.44761	0.80730	11.79	0.019	11.59	0.019	10.71	0.091	-	-	-	-	0
S345	0.45460	0.78185	13.01	0.029	12.70	0.035	-	-	-	-	-	-	0
S346	0.45168	0.79496	12.53	0.022	12.44	0.029	-	-	-	-	-	-	0
S347	0.45305	0.79645	13.74	0.034	13.48	0.059	-	-	-	-	-	-	0
S348	0.44216	0.82983	13.93	0.056	12.05	0.028	10.82	0.114	-	-	-	-	0
S349	0.43543	0.85750	12.51	0.027	12.28	0.028	10.61	0.095	-	-	-	-	0
S350	0.43680	0.85674	12.66	0.023	12.48	0.031	11.02	0.144	-	-	-	-	0
S351	0.43618	0.85561	13.05	0.026	12.78	0.037	-	-	-	-	-	-	0
S352	0.43765	0.85552	12.61	0.023	12.45	0.030	11.13	0.160	-	-	-	-	0
S353	0.43989	0.84478	14.01	0.041	13.35	0.044	-	-	-	-	-	-	0
S354	0.45041	0.80946	13.26	0.024	13.02	0.033	11.09	0.180	-	-	-	-	0
S355	0.45137	0.81115	14.11	0.036	13.80	0.062	-	-	-	-	-	-	0
S356	0.45484	0.79533	13.39	0.031	13.11	0.049	-	-	-	-	-	-	0
S357	0.44386	0.83757	14.04	0.043	13.63	0.061	-	-	-	-	-	-	0
S358	0.44362	0.83717	14.49	0.059	14.68	0.153	-	-	-	-	-	-	0
S359	0.45194	0.80682	14.04	0.037	13.47	0.052	-	-	-	-	-	-	0
S360	0.45055	0.81324	13.79	0.031	12.89	0.033	-	-	-	-	-	-	0
S361	0.45681	0.79031	13.98	0.038	13.63	0.061	-	-	-	-	-	-	0
S362	0.44820	0.82509	14.44	0.056	14.21	0.127	-	-	-	-	-	-	0
S363	0.43797	0.86732	12.15	0.022	12.07	0.027	11.39	0.183	-	-	-	-	0
S364	0.45391	0.80540	14.18	0.042	13.46	0.053	-	-	-	-	-	-	0
S365	0.44750	0.83284	14.73	0.065	14.29	0.108	-	-	-	-	-	-	0
S366	0.44225	0.86211	12.72	0.024	12.32	0.037	-	-	-	-	-	-	0
S367	0.44146	0.86085	12.46	0.022	12.15	0.029	-	-	-	-	-	-	0
S368	0.43961	0.86499	11.18	0.019	11.25	0.020	10.80	0.101	-	-	-	-	0
S369	0.45922	0.79027	13.24	0.026	13.04	0.036	-	-	-	-	-	-	0
S370	0.46052	0.79110	12.29	0.021	11.82	0.021	10.95	0.149	-	-	-	-	0
S371	0.46122	0.79213	10.95	0.018	11.00	0.019	9.99	0.063	-	-	-	-	0
S372	0.44915	0.82905	12.30	0.020	12.30	0.028	-	-	-	-	-	-	0
S373	0.44957	0.83083	10.92	0.018	11.11	0.019	10.38	0.077	-	-	-	-	0
S374	0.44398	0.84916	13.38	0.036	13.18	0.051	-	-	-	-	-	-	0
S375	0.44994	0.82780	13.77	0.035	13.70	0.079	-	-	-	-	-	-	0
S376	0.44786	0.83809	12.76	0.022	12.52	0.029	-	-	-	-	-	-	0
S377	0.44278	0.85761	14.54	0.070	14.41	0.153	-	-	-	-	-	-	0
S378	0.44474	0.85453	14.68	0.085	13.35	0.068	-	-	-	-	-	-	0
S379	0.45853	0.80401	11.87	0.019	11.16	0.019	10.71	0.150	-	-	-	-	0
S380	0.45015	0.83296	12.87	0.024	12.53	0.028	-	-	-	-	-	-	0
S381	0.44250	0.86531	11.23	0.022	10.68	0.018	10.12	0.054	-	-	-	-	0
S382	0.46206	0.78965	12.58	0.022	12.78	0.034	-	-	-	-	-	-	0
S383	0.46285	0.78624	13.08	0.029	13.08	0.042	-	-	-	-	-	-	0
S384	0.46104	0.79712	13.43	0.039	13.08	0.046	10.73	0.135	-	-	-	-	0
S385	0.44719	0.84908	13.28	0.031	13.29	0.060	-	-	-	-	-	-	0

continued on next page ...

Table 4. The complete list of merged point sources, continued.

name	RA -290 (degrees)	Dec. -13 (degrees)	[3.6] (mag)	$\sigma_{[3.6]}$ (mag)	[4.5] (mag)	$\sigma_{[4.5]}$ (mag)	[5.8] (mag)	$\sigma_{[5.8]}$ (mag)	[8.0] (mag)	$\sigma_{[8.0]}$ (mag)	[24] (mag)	$\sigma_{[24]}$ (mag)	ap. phot. flag
S386	0.44800	0.85127	12.46	0.032	11.24	0.021	10.98	0.149	-	-	-	-	0
S387	0.45010	0.84285	13.59	0.036	13.14	0.045	-	-	-	-	-	-	0
S388	0.45311	0.83254	14.10	0.046	13.22	0.049	-	-	-	-	-	-	0
S389	0.44910	0.84830	13.67	0.042	13.58	0.081	-	-	-	-	-	-	0
S390	0.44922	0.84875	14.03	0.053	13.68	0.089	-	-	-	-	-	-	0
S391	0.46308	0.79405	14.11	0.048	13.50	0.056	-	-	-	-	-	-	0
S392	0.45826	0.82334	14.80	0.070	14.05	0.099	-	-	-	-	-	-	0
S393	0.45066	0.85631	10.93	0.019	10.64	0.021	-	-	-	-	-	-	0
S394	0.44346	0.87080	12.93	0.033	12.81	0.049	-	-	-	-	-	-	0
S395	0.45911	0.81397	13.58	0.027	13.62	0.056	-	-	-	-	-	-	0
S396	0.45906	0.81320	14.08	0.035	13.99	0.105	-	-	-	-	-	-	0
S397	0.45101	0.84868	12.37	0.021	12.34	0.031	-	-	-	-	-	-	0
S398	0.45455	0.84859	13.25	0.029	13.05	0.052	-	-	-	-	-	-	0
S399	0.45577	0.85061	13.07	0.030	12.87	0.056	-	-	-	-	-	-	0
S400	0.45433	0.85269	12.81	0.028	12.81	0.060	-	-	-	-	-	-	0
S401	0.45029	0.85012	13.55	0.039	13.45	0.080	-	-	-	-	-	-	0
S402	0.45105	0.84946	14.23	0.062	14.25	0.165	-	-	-	-	-	-	0
S403	0.46726	0.79131	12.94	0.035	12.39	0.032	-	-	-	-	-	-	0
S404	0.46461	0.80327	12.02	0.028	11.10	0.019	10.33	0.097	-	-	-	-	0
S405	0.46600	0.80099	10.43	0.018	10.04	0.017	8.40	0.022	-	-	-	-	0
S406	0.46868	0.80087	12.91	0.023	12.62	0.029	-	-	-	-	-	-	0
S407	0.45538	0.84661	13.22	0.035	13.34	0.067	11.33	0.167	-	-	-	-	0
S408	0.44927	0.86721	13.60	0.040	13.33	0.067	-	-	-	-	-	-	0
S409	0.46932	0.79116	13.22	0.025	13.23	0.042	-	-	-	-	-	-	0
S410	0.46015	0.82931	13.21	0.025	12.34	0.026	-	-	-	-	-	-	0
S411	0.45167	0.86156	12.72	0.029	12.24	0.039	-	-	-	-	-	-	0
S412	0.45818	0.83702	11.11	0.018	11.35	0.019	10.90	0.115	-	-	-	-	0
S413	0.45941	0.83332	12.82	0.025	11.92	0.023	11.35	0.175	-	-	-	-	0
S414	0.44972	0.87089	13.19	0.031	13.19	0.062	-	-	-	-	-	-	0
S415	0.45414	0.85634	12.76	0.030	12.84	0.070	-	-	-	-	-	-	0
S416	0.45504	0.85640	12.96	0.034	12.84	0.070	-	-	-	-	-	-	0
S417	0.45499	0.85539	12.73	0.028	12.65	0.059	-	-	-	-	-	-	0
S418	0.45618	0.85514	12.57	0.026	12.37	0.044	-	-	-	-	-	-	0
S419	0.46760	0.80637	10.86	0.018	10.99	0.018	9.42	0.038	-	-	-	-	0
S420	0.46005	0.83754	13.67	0.039	12.79	0.038	-	-	-	-	-	-	0
S421	0.46709	0.81142	13.89	0.033	13.53	0.051	-	-	-	-	-	-	0
S422	0.46434	0.82431	12.76	0.021	12.70	0.031	-	-	-	-	-	-	0
S423	0.46497	0.82517	13.45	0.027	13.22	0.045	-	-	-	-	-	-	0
S424	0.45449	0.86534	10.88	0.019	11.01	0.021	10.17	0.061	-	-	-	-	0
S425	0.46011	0.86711	12.20	0.022	12.27	0.035	11.04	0.132	-	-	-	-	0
S426	0.46246	0.83069	14.32	0.048	14.09	0.093	-	-	-	-	-	-	0
S427	0.46708	0.81511	13.75	0.030	13.62	0.052	-	-	-	-	-	-	0
S428	0.46700	0.81642	13.58	0.028	13.61	0.050	-	-	-	-	-	-	0
S429	0.46278	0.83282	13.66	0.034	13.51	0.060	11.72	0.220	-	-	-	-	0
S430	0.46187	0.84059	11.93	0.019	11.93	0.022	10.25	0.052	-	-	-	-	0
S431	0.46483	0.84394	12.26	0.021	12.21	0.027	11.57	0.196	-	-	-	-	0
S432	0.45943	0.84986	14.20	0.057	13.94	0.118	-	-	-	-	-	-	0
S433	0.45409	0.87148	11.99	0.024	11.72	0.025	10.84	0.110	-	-	-	-	0
S434	0.47565	0.78805	13.54	0.041	13.09	0.048	-	-	-	-	-	-	0
S435	0.46500	0.83078	12.80	0.024	12.50	0.029	11.06	0.121	-	-	-	-	0
S436	0.47132	0.81355	10.53	0.017	10.61	0.017	10.07	0.049	-	-	-	-	0
S437	0.47350	0.80157	13.98	0.038	13.44	0.050	-	-	-	-	-	-	0
S438	0.46254	0.84674	13.76	0.041	13.38	0.066	-	-	-	-	-	-	0
S439	0.46520	0.83617	13.85	0.038	13.75	0.082	-	-	-	-	-	-	0
S440	0.46128	0.85555	12.72	0.023	12.53	0.036	-	-	-	-	-	-	0
S441	0.46186	0.85687	12.84	0.026	12.09	0.027	10.79	0.091	-	-	-	-	0
S442	0.46681	0.83648	13.44	0.036	12.53	0.031	-	-	-	-	-	-	0
S443	0.46379	0.84810	11.83	0.019	11.82	0.024	-	-	-	-	-	-	0
S444	0.46486	0.84994	12.43	0.021	12.33	0.029	-	-	-	-	-	-	0
S445	0.45717	0.87435	-	-	13.15	0.057	11.54	0.219	-	-	-	-	0
S446	0.46930	0.82971	13.51	0.031	13.09	0.042	-	-	-	-	-	-	0
S447	0.46708	0.84032	12.35	0.021	12.32	0.027	10.85	0.093	-	-	-	-	0
S448	0.46233	0.86069	13.18	0.032	12.97	0.050	-	-	-	-	-	-	0
S449	0.47486	0.81091	14.61	0.059	13.62	0.054	-	-	-	-	-	-	0
S450	0.47470	0.81380	13.87	0.034	13.70	0.052	-	-	-	-	-	-	0

continued on next page ...

Table 4. The complete list of merged point sources, continued.

name	RA -290 (degrees)	Dec. -13 (degrees)	[3.6] (mag)	$\sigma_{[3.6]}$ (mag)	[4.5] (mag)	$\sigma_{[4.5]}$ (mag)	[5.8] (mag)	$\sigma_{[5.8]}$ (mag)	[8.0] (mag)	$\sigma_{[8.0]}$ (mag)	[24] (mag)	$\sigma_{[24]}$ (mag)	ap. phot. flag
S451	0.46678	0.84585	12.16	0.021	12.14	0.028	-	-	-	-	-	-	0
S452	0.46749	0.84520	12.16	0.021	12.12	0.027	11.25	0.164	-	-	-	-	0
S453	0.48003	0.79620	11.79	0.019	11.82	0.021	10.79	0.113	-	-	-	-	0
S454	0.46629	0.84775	13.65	0.039	13.55	0.080	-	-	-	-	-	-	0
S455	0.46061	0.87007	13.54	0.040	13.12	0.069	-	-	-	-	-	-	0
S456	0.46533	0.85311	13.41	0.038	13.38	0.064	11.48	0.188	-	-	-	-	0
S457	0.46206	0.86766	12.54	0.024	12.40	0.039	11.42	0.199	-	-	-	-	0
S458	0.48035	0.79929	11.13	0.018	11.29	0.019	10.15	0.058	-	-	-	-	0
S459	0.48156	0.80023	13.16	0.025	13.05	0.038	-	-	-	-	-	-	0
S460	0.47897	0.80553	13.58	0.032	13.45	0.049	-	-	-	-	-	-	0
S461	0.47877	0.81356	12.68	0.022	12.55	0.027	11.10	0.120	-	-	-	-	0
S462	0.47209	0.83589	13.31	0.033	13.16	0.045	-	-	-	-	-	-	0
S463	0.47349	0.83532	12.41	0.022	12.32	0.027	-	-	-	-	-	-	0
S464	0.47437	0.83428	14.31	0.054	13.60	0.065	-	-	-	-	-	-	0
S465	0.46402	0.86988	12.47	0.025	12.46	0.041	-	-	-	-	-	-	0
S466	0.47169	0.84052	13.55	0.034	13.38	0.057	-	-	-	-	-	-	0
S467	0.47127	0.84378	12.26	0.023	11.95	0.025	10.88	0.115	-	-	-	-	0
S468	0.46871	0.85522	13.18	0.035	12.91	0.044	-	-	-	-	-	-	0
S469	0.48408	0.79857	12.39	0.031	11.53	0.021	-	-	-	-	-	-	0
S470	0.47071	0.85011	13.72	0.039	13.61	0.081	-	-	-	-	-	-	0
S471	0.47151	0.85068	14.38	0.061	13.98	0.134	-	-	-	-	-	-	0
S472	0.46904	0.86051	12.32	0.023	11.94	0.027	10.39	0.085	-	-	-	-	0
S473	0.48474	0.80199	12.68	0.024	12.50	0.030	11.16	0.142	-	-	-	-	0
S474	0.48524	0.80090	11.99	0.022	11.98	0.024	-	-	-	-	-	-	0
S475	0.47440	0.84359	12.15	0.023	11.72	0.023	10.80	0.116	-	-	-	-	0
S476	0.47505	0.84221	12.26	0.022	12.23	0.027	-	-	-	-	-	-	0
S477	0.47189	0.85164	12.69	0.025	12.59	0.036	-	-	-	-	-	-	0
S478	0.48657	0.79656	12.29	0.023	12.34	0.029	10.95	0.161	-	-	-	-	0
S479	0.47247	0.85392	11.92	0.021	11.85	0.025	-	-	-	-	-	-	0
S480	0.47345	0.85391	12.56	0.027	12.41	0.035	-	-	-	-	-	-	0
S481	0.47431	0.85334	12.97	0.033	12.68	0.040	-	-	-	-	-	-	0
S482	0.48064	0.82827	10.11	0.019	10.30	0.020	9.68	0.043	-	-	-	-	0
S483	0.48577	0.80905	12.97	0.034	12.49	0.031	-	-	-	-	-	-	0
S484	0.48287	0.82162	13.93	0.063	13.91	0.113	-	-	-	-	-	-	0
S485	0.48261	0.82106	13.68	0.054	13.00	0.048	-	-	-	-	-	-	0
S486	0.48323	0.82194	13.39	0.039	13.06	0.049	-	-	-	-	-	-	0
S487	0.47351	0.85647	12.95	0.032	12.81	0.046	-	-	-	-	-	-	0
S488	0.47318	0.85746	13.91	0.060	12.87	0.049	-	-	-	-	-	-	0
S489	0.47426	0.85491	12.78	0.031	12.48	0.037	-	-	-	-	-	-	0
S490	0.47163	0.86855	14.18	0.078	12.55	0.043	10.79	0.163	-	-	-	-	0